Journal of Catalysis 368 (2018) 38–52

Contents lists available at ScienceDirect

Journal of Catalysis

journal homepage: www.elsevier.com/locate/jcat

Enhanced lattice oxygen reactivity over Fe_2O_3/Al_2O_3 redox catalyst for chemical-looping dry (CO_2) reforming of CH_4: Synergistic La-Ce effect

Mingchen Tang [a], Kuo Liu [b,d], Dean M. Roddick [a], Maohong Fan [b,c,*]

[a] Department of Chemistry, University of Wyoming, Laramie, WY 82071, USA
[b] Chemical & Petroleum Engineering, University of Wyoming, Laramie, WY 82071, USA
[c] School of Energy Resources, University of Wyoming, Laramie, WY 82071, USA
[d] Research Center for Eco-Environment Sciences, Chinese Academy of Sciences, Beijing 100085, PR China

ARTICLE INFO

Article history:
Received 11 April 2018
Revised 19 September 2018
Accepted 23 September 2018
Available online 13 October 2018

Keywords:
Chemical-looping
Partial oxidation of CH_4
CO_2 reduction
Syngas production
Synergistic La-Ce effect
Redox catalyst
Perovskite-type solid solution

ABSTRACT

Chemical-looping dry (CO_2) reforming (CLDR) of CH_4 over the La_xCe_{1-x}-Fe_2O_3/Al_2O_3 (x = 0, 0.33, 0.67, and 1) redox catalysts paves a novel path for efficient syngas production and intensive CO_2 reduction. The isolation of CO_2 splitting (CS) from partial oxidation of CH_4 (POM) via the proposed CLDR process makes it possible to economically address the carbon deposition of significant concern in conventional dry reforming and other related applications, and meanwhile enable a straightforward determination of active phases involved in the cyclic CLDR operation. Owing to the rare earth (i.e., La and Ce) incorporations and intimate contacts among the active Fe species, a large amount of perovskite ($LaFeO_3$ and $CeFeO_3$)-derived oxygen defects along with CeO_2-assisted surface dispersion improvement hammer out tunnels beneficial for lattice oxygen migration, hence constituting the synergistic La-Ce effect. Moreover, our findings reveal that such La-Ce effect is advantageous for enhancing the resistance of Fe_2O_3/Al_2O_3 redox catalyst toward particle sintering and formation of inactive carbon, which guarantees catalyst tolerance against accumulated carbon deposition and more importantly the effective CO_2 activation for both lattice oxygen replenishment and carbon removal. Herein, our findings demonstrate the potential of utilizing La_xCe_{1-x}-Fe_2O_3/Al_2O_3 (x = 0.33) as a most promising redox catalyst for the proposed CLDR process.

1. Introduction

The Paris climate agreement, which aims to limit the global temperature increase to 1.5–2 °C relative to pre-industrial levels, has significantly heightened the urgency in CO_2 emission control [1–5]. However, the current and emerging CO_2 capture and storage options may fall in line with the industrial goal of minimizing the energy cost and ensuring the competitiveness [6–9]. Alternatively, the technology roadmap of CO_2 utilization is of specific importance, for its capability of converting CO_2 into significant profitable benefits such as chemicals, cement, or plastics, by thermal [10–12], photocatalytic [13,14], electrocatalytic [15], and biochemical [16] strategies. Considerable attention has long been paid to CO_2/CH_4 reforming reaction (also known as dry reforming) ($CO_2 + CH_4 \rightarrow 2CO + 2H_2, \Delta H_{298K} = 247 kJ \cdot mol^{-1}$) produces synthesis gas, or syngas with a low H_2/CO ratio, which is desirable for subsequent ammonia or methanol synthesis and preferential for the selectivity of long-chain hydrocarbons via Fischer-Tropsch process [17]. Nonetheless, conventional dry reforming suffers from the severe catalyst deactivation caused by carbon deposition [18,19]. Extensive research efforts have been devoted to the development of carbon-resistant catalysts and the optimization of catalyst regeneration process to offset the adverse influence of carbon deposition [20–22]. In the former case, the methodologies including tailoring active metal particle properties (i.e., size, shape, and structure) and introducing noble metal (i.e., Rh, Ru, Pt, and Pd) and/or alkaline metal additives, etc., are either costly or at the expense of sacrificing the catalyst activity [17]. In the latter case, a "mixed" reforming by co-feeding steam and/or O_2 can improve the carbon resistance of catalysts but results in an increased operating cost (i.e., steam generation, cryogenic air separation) up to 20% [17]. To date, carbon deposition remains to be a primary obstacle to the industrial realization of dry reforming process.

Neal et al. [23] reported the use of air for the regeneration of redox catalysts via chemical-looping reforming, by the mean of which the depleted lattice oxygen (O^{2-}) during CH_4 oxidation in one reactor (reducer) gets replenished from air in the other reactor (oxidizer). The avoidance of direct contact between CH_4 and

* Corresponding author at: Chemical & Petroleum Engineering, University of Wyoming, Laramie, WY 82071, USA.
E-mail address: mfan@uwyo.edu (M. Fan).

https://doi.org/10.1016/j.jcat.2018.09.022
0021-9517/

oxygen-supplying reagent (e.g., air) enables a reduction in energy consumption and meanwhile an increase in CH_4 conversion efficiency, demonstrating that chemical-looping technology is of great applicable importance [24,25]. Sharing the similar idea, Veser's group proposed and realized the chemical-looping based reverse water–gas shift reaction ($CO_2 + H_2 \rightarrow CO + H_2O$) which allows intensive and effective CO_2 reduction and simultaneously H_2 conversion as a model fuel [26]. Herein, our present contribution was motivated to combine CH_4 oxidation and CO_2 reduction under the chemical-looping regime [27] and to orient the resulting configuration for the industrially important syngas production. Although the net reaction of chemical-looping dry (CO_2) reforming (CLDR) coincides with that of conventional dry reforming reaction, CLDR process carried out in a typical circulating fluidized-bed configuration has profound technical advantages in the following aspects, e.g. capable of handling dilute CO_2 streams under any circumstances which redox catalysts are inert to the other present gas components [26], controllable reduction degrees of redox catalysts while avoiding the occurrence of carbon deposition, and governable H_2/CO ratios by flexibly adjusting the flow rate of feedstocks and the circulating rate of looping particles [28], etc. Although a similar concept of CLDR has been proposed in the previous literature [28], CLDR application optimized for syngas production via a simultaneous utilization of CO_2 and CH_4 is rarely reported.

Due to the CLDR nature which isolates CH_4 oxidation from CO_2 reduction, it is vital to design and engineer redox catalysts with not only excellent lattice oxygen reactivity (i.e., fast reaction kinetics relying on material composition, particle size, porosity, shape, structure and specific surface area) and operation stability (i.e., carbon deposition, thermal, and attrition resistance) but also high practical prospects from cost-effective and environmental-benign perspectives [29]. Among various investigated transition metals ('M') (e.g. Mo, Cr, Fe, Zn, Co, Nb, etc.), oxygen-depleted Fe-based oxides are attractive candidates for CO_2 splitting (CS) ($M + CO_2 \rightarrow MO + CO$) because of the large oxygen storage capacity from CO_2 (0.7 mol of CO_2 per mol of Fe) over a broad operating temperature window (700–1800 °C) [26]. However, a typical reduction of pure Fe oxides undergoes step-wise phase transition (Fe_2O_3, hematite → Fe_3O_4, magnetite → FeO, fcc → Fe, bcc) induced lattice structure arrangement, which forms dense oxide overlayers severely retarding the reduction kinetics and limiting the accessibility of bulk Fe phase. Accordingly, depending on the reactivity of available free oxygen species on redox catalysts, extended metal oxide exposure to CH_4 sequentially carries out complete oxidation of CH_4 (COM) ($4MO + CH_4 \rightarrow 4M + CO_2 + 2H_2O$), partial oxidation of CH_4 (POM) ($MO + CH_4 \rightarrow M + 2H_2 + CO$), and pyrolysis of CH_4 ($CH_4 \rightarrow C + 2H_2, \Delta H_{298K} = 74.6 kJ \cdot mol^{-1}$) [30–36]. Limited to thermodynamic constraints, phase transition from Fe_2O_3 to Fe_3O_4 is prone to COM, while POM is more favored during the FeO → Fe transition [37]. Hence, it is essentially critical to enhance the lattice oxygen mobility for facilitating syngas production and maximizing POM selectivity, as well as increasing the reactivity of redox catalyst toward CS reaction.

Recently, there have been ever-increasing interests in structural engineering of Fe-based oxides, especially considering perovskite-type solid solution as building blocks [38]. Perovskites such as lanthanum orthoferrite ($LaFeO_3$) [23,39–44] and cerium orthoferrite ($CeFeO_3$) [45–49] are often designed as the active sites for catalytic CH_4 conversion into syngas [45,50]. Despite the improved oxygen mobility, perovskite-type oxides suffer from the low specific surface area. In this regard, a three-dimensionally ordered macroporous $LaFeO_3$ with higher surface area was reported, which exhibits better reactivity toward CH_4 oxidation than $LaFeO_3$ nanopowder [42]. The combination of perovskite-type oxides and metal oxides such as CeO_2 [50] and Fe_2O_3 [43] can lead to a high surface area and multiple catalytic performance benefits [50,51]. Zheng et al. [50] reported the design which CeO_2 is supported on macroporous $LaFeO_3$, and applied this redox catalyst for chemical-looping reforming of CH_4. It was suggested that Fe^{2+} or Ce^{3+} on the CeO_2-$LaFeO_3$ interface should be the active sites of CH_4 oxidation [50]. Neal et al. [23] developed Fe_2O_3@$La_{0.8}Sr_{0.2}FeO_{3-\delta}$ core-shell redox catalyst and found the perovskite shell gives the active sites and responsible for the acceleration of oxygen conduction, while the Fe-oxide core primarily supplies the lattice oxygen. In summary, the nowadays research focus is still on the development of perovskite-type oxides with higher oxygen mobility and larger surface area. Besides, the findings in the active metal species of redox catalysts comprising of La, Ce, and Fe would certainly illuminate the future design of catalytically efficient looping materials.

In these regards, our study was enlightened to alter the perspective on carbon deposition induced catalyst deactivation to the respect of carbon, i.e., as an active chemical-looping intermediate contributing to intensive CO_2 reduction for CO evolution. Also, high-surface-area redox catalysts (La_xCe_{1-x}-Fe_2O_3/Al_2O_3) comprising of $LaFeO_3$ perovskite and oxidized Ce and Fe species were developed, and their performance in catalyzing CLDR was evaluated in the present work. Through a series of surface characterizations, the active phases and the reaction pathways reflecting the redox behavior of La_xCe_{1-x}-Fe_2O_3/Al_2O_3 catalysts were determined, beneficial for an in-depth rational understanding of the synergistic La-Ce effect on improving the lattice oxygen mobility and carbon resistance of Fe_2O_3/Al_2O_3 during cyclic CLDR operation.

2. Experimental section

2.1. Synthesis of La_xCe_{1-x}-Fe_2O_3/Al_2O_3 redox catalysts

La_xCe_{1-x}-Fe_2O_3/Al_2O_3 (x = 0, 0.33, 0.67, and 1) redox catalysts were prepared via a co-precipitation method, and the catalyst compositions are listed in Table 1. The following chemicals were used as the ingredients: $Fe(NO_3)_3{\cdot}9H_2O$ (Sigma-Aldrich, ≥98%), $Ce(NO_3)_3{\cdot}6H_2O$ (Sigma-Aldrich, 99.99%, trace metal basis), $La(NO_3)_3{\cdot}6H_2O$ (Fluka, ≥99.0%), and γ-Al_2O_3 (Alfa Aesar, 99.5%, metal basis). In the beginning, a predetermined amount of metallic nitrate salts was dissolved in de-ionized H_2O, while the γ-Al_2O_3 support was well-dispersed in diluted NH_4OH (EMD, 14.8M). Then, under continuous ultrasonication (Qsonica, Q700), the nitrate solution was dropwise injected into the evenly spread turbid liquid (γ-Al_2O_3 dispersed in NH_4OH solution) to form precipitates. Subsequently, the resulting mixture was subjected to freeze-drying (Labconco, FreeZone) for H_2O removal via sublimation, which approximately takes 72 h. The dehydrated material was calcined in air at 900 °C for 6 h. After finely crushing and sieving of the thermally treated powder, the catalyst particles were obtained with a diameter size less than 180 μm. For comparison, Fe_2O_3/Al_2O_3 was also prepared by following the same procedure.

2.2. Reactivity and stability evaluation

Conceptually, the industrial realization of CLDR process via a typical circulating fluidized-bed configuration is shown in Fig. S1. While on a laboratory scale, the proposed CLDR process was carried out in a fixed-bed reactor configuration as presented in Fig. 1. A quartz reactor (4 mm in inner diameter, and 54 cm in length) was vertically mounted inside a tubular furnace (Carbolite, TVS). The actual reaction temperature was monitored at the center position of the catalyst packing bed by a K-type thermocouple. The temperature variance between the furnace and the reactor was maintained at a reasonable range (3.5–4.5 °C). The experimental setup was adopted to evaluate the catalyst performance during

Table 1
Compositions and general surface characteristics of the prepared redox catalysts.

Property		Fe_2O_3/Al_2O_3	La_xCe_{1-x}-Fe_2O_3/Al_2O_3			
			x = 0	x = 0.33	x = 0.67	x = 1
Content (wt.%)	Fe_2O_3	43	30	30	30	30
	CeO_2	0	30	20	10	0
	La_2O_3	0	0	10	20	30
	Al_2O_3	57	40	40	40	40
BET surface area (m^2/g)		13.385	13.283	56.213	55.939	49.726
BJH pore volume (cm^3/g)		0.200	0.243	0.291	0.289	0.251
Active metal surface area (m^2/g)	Per gram of sample	0.346	0.649	0.694	0.507	0.229
	Per gram of metal	26.153	49.077	52.518	38.358	17.288
Percent metal dispersion (%)		3.953	7.418	7.938	5.798	2.613
Average crystalline size (Å)		291.878	155.543	145.352	199.011	441.564
Monolayer uptake of H_2 (μmol/g_{cat})		4.677	8.777	9.393	6.860	3.092

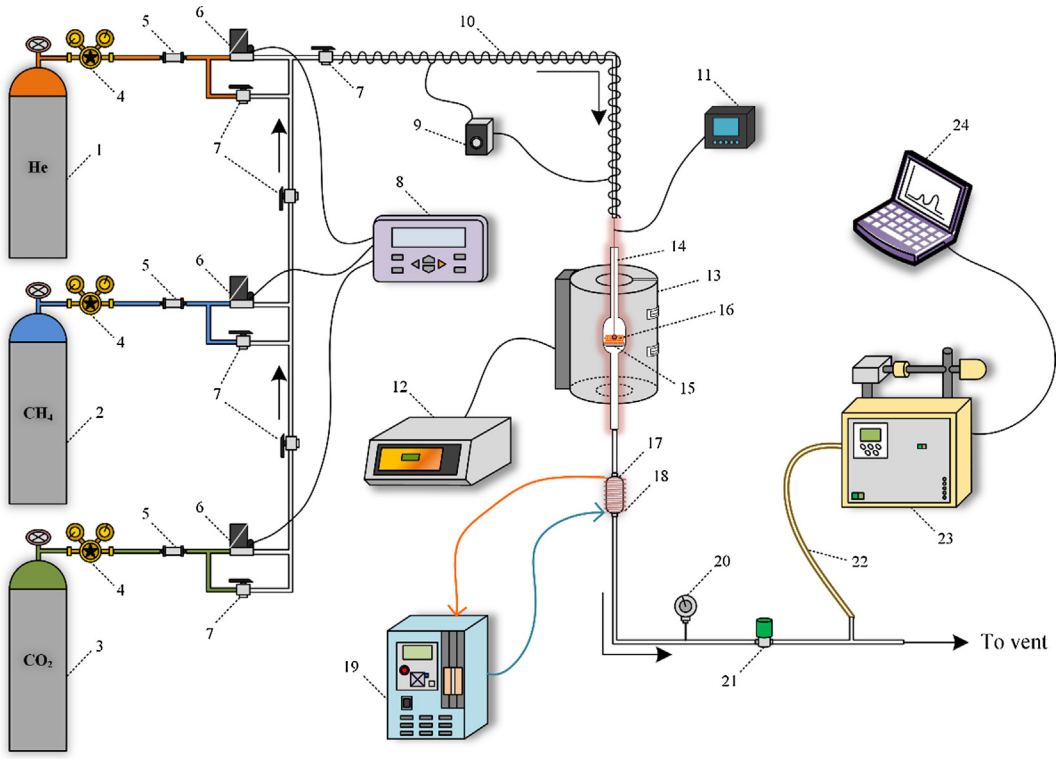

Fig. 1. Experimental setup for CLDR process: (1) He cylinder; (2) CH_4 cylinder; (3) CO_2 cylinder; (4) pressure regulator; (5) filter; (6) mass flow controller; (7) valve; (8) mass flow control box; (9) converter; (10) heating tape; (11) temperature scanner; (12) furnace control unit; (13) tubular furnace; (14) quartz reactor; (15) frits; (16) catalyst packing bed; (17) water trap; (18) copper tube; (19) chiller; (20) pressure indicator; (21) back pressure regulator; (22) capillary liner; (23) mass spectrometer; (24) data acquisition unit.

CH_4 oxidation and CO_2 reduction as well as the successive 10 redox cycles. At the onset of each test, a sample size of 0.1 g was placed in the center of this reactor and heated to the designed temperature conditions (750, 800, and 850 °C) at 5 °C/min under a constant flow of 20 ml/min He. By mean of the LabVIEW system design software (National Instrument), solid redox catalyst particles can be kept stationary and alternately exposed to the reducing and oxidizing environment by periodically switching the CH_4 (2 ml/min) and CO_2 (2 ml/min) feed as programmed, therefore realizing the automatic cyclic CLDR operation. Before switching the redox environment, the reactor was purged under He for 1 h to assure well-defined conditions at the beginning of each half-cycle. A mass spectrometer (Hiden, HPR-20 QIC) was connected to analysis the effluent gas compositions.

A carbon balance was performed for each data point obtained during the CH_4 oxidation step to assure the accuracy of the analysis, where errors up to 5–10% were acceptable in view of the precision of the calibration factor for all reported experiments.

$$n_{CH_4,in} = n_{CH_4,out} + n_{CO_2,out} + n_{CO,out} + 0.5 * (n_{H_2,out} - 2 * n_{CO,out}) \quad (E1)$$

where $n_{CH_4,in}$ is the molar flow rate of CH_4 in the inlet feed stream; whilen$_{CH_4,out}$, $n_{H_2,out}$, $n_{CO,out}$, and $n_{CO_2,out}$ are the molar flow rate of CH_4, H_2, CO, and CO_2 in the effluents, respectively. Moreover, the expression of $0.5 * (n_{H_2,out} - 2 * n_{CO,out})$ was regarded as the quantitative calculation for carbon deposition, n_{Carbon}.

The total amount of oxygen participating in CH_4 oxidation can be calculated using the following expression:

$$n_{Oxygen} = 4 * n_{CO_2,out} + n_{CO,out} \quad (E2)$$

The CH_4 conversion (X_{CH_4}) and CO selectivity (S_{CO}) during CH_4 oxidation, and CO_2 conversion (X_{CO_2}) during CO_2 reduction were calculated according to the following equations:

$$X_{CH_4} = \frac{n_{CH_4,in} - n_{CH_4,out}}{n_{CH_4,in}} \quad (E3)$$

$$S_{CO} = \frac{n_{CO,out}}{n_{CH_4,in} - n_{CH_4,out}} \quad (E4)$$

$$X_{CO_2} = \frac{n_{CO_2,in} - n_{CO_2,out}}{n_{CO_2,in}} \quad (E5)$$

2.3. Characterization of La_xCe_{1-x}-Fe_2O_3/Al_2O_3 redox catalysts

The reducibility and oxidizability of the redox catalysts were investigated using temperature-programmed reduction (TPR) and oxidation (TPO), respectively. While H_2-TPR was realized using the Autosorb-iQ system (Quantachrome), CH_4-TPR and CO_2-TPO were conducted in the same fixed-bed quartz reactor configuration described earlier. For each temperature-programmed experiment, a sample size of 0.1 g was used for each run. Prior to H_2-TPR and CH_4-TPR experiments, the fresh catalysts (after calcination) were outgassed using 20 ml/min He at 500 °C for 1 h. As soon as the sample was cooled down to room temperature, a flow of 2 ml/min reacting gas (H_2 or CH_4) balanced with 20 ml/min He was introduced to the reactor. In the case of CO_2-TPO, the fresh catalysts were pre-reduced using 2 ml/min H_2 (or CH_4) balanced with 20 ml/min He at 850 °C for 1 h, followed by cooling to the ambient under pure He. Subsequently, a flow of 2 ml/min CO_2 diluted in 20 ml/min He was fed into the reactor for 1 h of CO_2 adsorption. For all the temperature-programmed experiments, a constant heating rate of 5 °C/min was applied.

The specific surface area of the fresh catalysts was measured through N_2-adsorption/desorption at −196 °C using a Brunauer-Emmett-Teller (BET) analyzer (Quantachrome, Autosorb-iQ). The samples were outgassed at 200 °C under vacuum for 2 h to eliminate volatile adsorbates on the surface, before the analysis. The Barrett-Joyner-Halenda (BJH) desorption method was applied to calculate the pore size distribution of each sample.

H_2-chemisorption tests were also performed using this multifunctional surface characterization instrument (Quantachrome, Autosorb-iQ). The fresh catalysts were outgassed under pure He environment at 500 °C for 1 h, followed by reduction at 850 °C using 5% H_2/He. After the evacuation (10^{-6} torr for 30 min) of the reduced catalysts at 850 °C, the samples were cooled down to the room temperature. Irreversible H_2 uptakes for the reduced catalysts were then obtained from the total and reversible adsorption isotherms taken in a pressure range of 50–300 mm Hg.

The crystal phases of the fresh and used (after cyclic redox treatment) catalysts were obtained with an X-ray diffraction (XRD) system (Rigaku, Smartlab) using Cu Kα radiation at 40 kV and 40 mA. The 2θ scanning range was chosen from 20° to 80°, and the scanning rate was 1°/min.

The X-ray photoelectron spectroscopy (XPS) spectra for both the fresh and used catalysts were collected using an ultra-delay line detector (Kratos, Axis) equipped with a monochromatic Al Kα X-ray source, and a hemispherical/spherical analyzer that is capable of the parallel spectrum and imaging. The X-ray source was run at 10 mA and 15 kV. High-resolution scans were collected using a pass energy of 40 eV with a step size of 0.1 eV. The binding energies were calibrated based on the C1s peak at 284.8 eV as a reference.

3. Results and discussions

3.1. CLDR performance Evaluation of La_xCe_{1-x}-Fe_2O_3/Al_2O_3 redox catalysts

The CH_4 oxidation experiments (Fig. 2) were carried out to investigate the effect of temperature on the lattice oxygen selectivity toward POM concerning the CO evolution. Although the La-free catalysts, Fe_2O_3/Al_2O_3 and the modified catalyst (x = 0), exhibited more accumulated CO evolution at 800 and 850 °C within the 60-min time-on-stream, the POM reaction proceeded much slower over these two catalysts than the three La-loaded ones (especially for the modified catalyst (x = 1)). Usually, lattice oxygen is more selective to POM than surface-adsorbed oxygen [45]. Therefore, it can be inferred that Fe_2O_3/Al_2O_3 and the modified catalyst (x = 0) possessed a more substantial proportion of lattice oxygen but are less reactive towards POM compared with the La-loaded catalysts. At an even lower temperature of 750 °C, more severe hysteresis took place for both the modified catalyst (x = 0) and Fe_2O_3/Al_2O_3, suggesting an inhibited oxygen mobility in the absence of La-introduction. At higher temperatures, the hysteresis in POM for Fe_2O_3/Al_2O_3 and the modified catalyst (x = 0) tend to be alleviated, mainly owing to the increased oxygen mobility by thermodynamic driving force [52].

Due to the intentionally prolonged catalyst exposure in the CH_4 environment and the as-induced occurrence of catalyzed CH_4 pyrolysis [18] over oxygen-depleted catalyst surface, significant carbon deposition is of great concern for the subsequent catalyst regeneration process. In a situation free of deposited carbon, the CO evolution via CS reaction is merely determined by the availability and accessibility of oxygen vacancies. Hence, owing to the contribution by carbon removal using CO_2 ($CO_2 + C \rightarrow 2CO$, $\Delta H_{298K} = 172.5 kJ \cdot mol^{-1}$) [21,22], the amount of CO evolution during the actual CO_2 reduction step should far exceed that generated via POM during the CH_4 oxidation process over all the examined catalysts. Fig. 2 also presents the CO evolution trajectory for the reduced catalysts during CO_2 reduction at different temperatures. The lower-temperature (750 °C) profiles for Fe_2O_3/Al_2O_3 and the modified catalyst (x = 0) show evidently smaller CO evolution than those for the La-loaded catalysts, which is by the incomplete CH_4 oxidation due to the relatively low oxygen mobility and meanwhile suggests an absence of deposited carbon. In this case, the limiting factor for oxygen replenishment of Fe_2O_3/Al_2O_3 and the modified catalyst (x = 0) may be the surface oxygen exchange kinetics involving both the oxygen reduction reaction and the bulk ion mobilization [53]. Comparably, benefiting from the Ce-incorporation, the reduced modified catalyst (x = 0) exhibits a lot faster oxygen exchange kinetics than Fe_2O_3/Al_2O_3. At higher temperatures (800 and 850 °C), thermodynamically favored CO_2 removal of carbon and improved oxygen mobility give rise to the amount of CO_2 reduced. Hence, the adsorption of CO_2 and the reactivity of carbonaceous species over the reduced catalyst surface add up to the kinetic-limiting factors and certainly would complicate the actual overall CO_2 reduction step. Diffusive reflectance infrared Fourier transform (DRIFT) experiments (Fig. S2) were carried out and confirmed that in a carbon deposition-free situation the oxygen replenishment of catalyst could proceed in the absence of surface pre-adsorption of CO_2 above 500 °C. Therefore, carbon deposition remains to play a critical role in CLDR operation while assuring efficient redox kinetics of catalysts and sufficiently high syngas production.

Since all the prepared catalysts exhibit a complete profile for CO evolution via POM at 800 °C, the evaluation of catalyst activity concerning the 10-cycle CLDR performance can be continuously conducted at 800 °C. Fig. 3 shows the variation of CH_4 conversion and CO selectivity for the CH_4 oxidation step from cycle to cycle. Among the examined catalysts, Fe_2O_3/Al_2O_3 gives the highest CH_4 conversion (92.23%) and CO selectivity (10.14%) during the 10th cycle of CH_4 oxidation. However, compared with the modified catalysts, a substantial decline in CO selectivity appeared after the 1st-cycle use of Fe_2O_3/Al_2O_3, suggesting a remarkable loss in the available POM-favored lattice oxygen. The reduced lattice oxygen

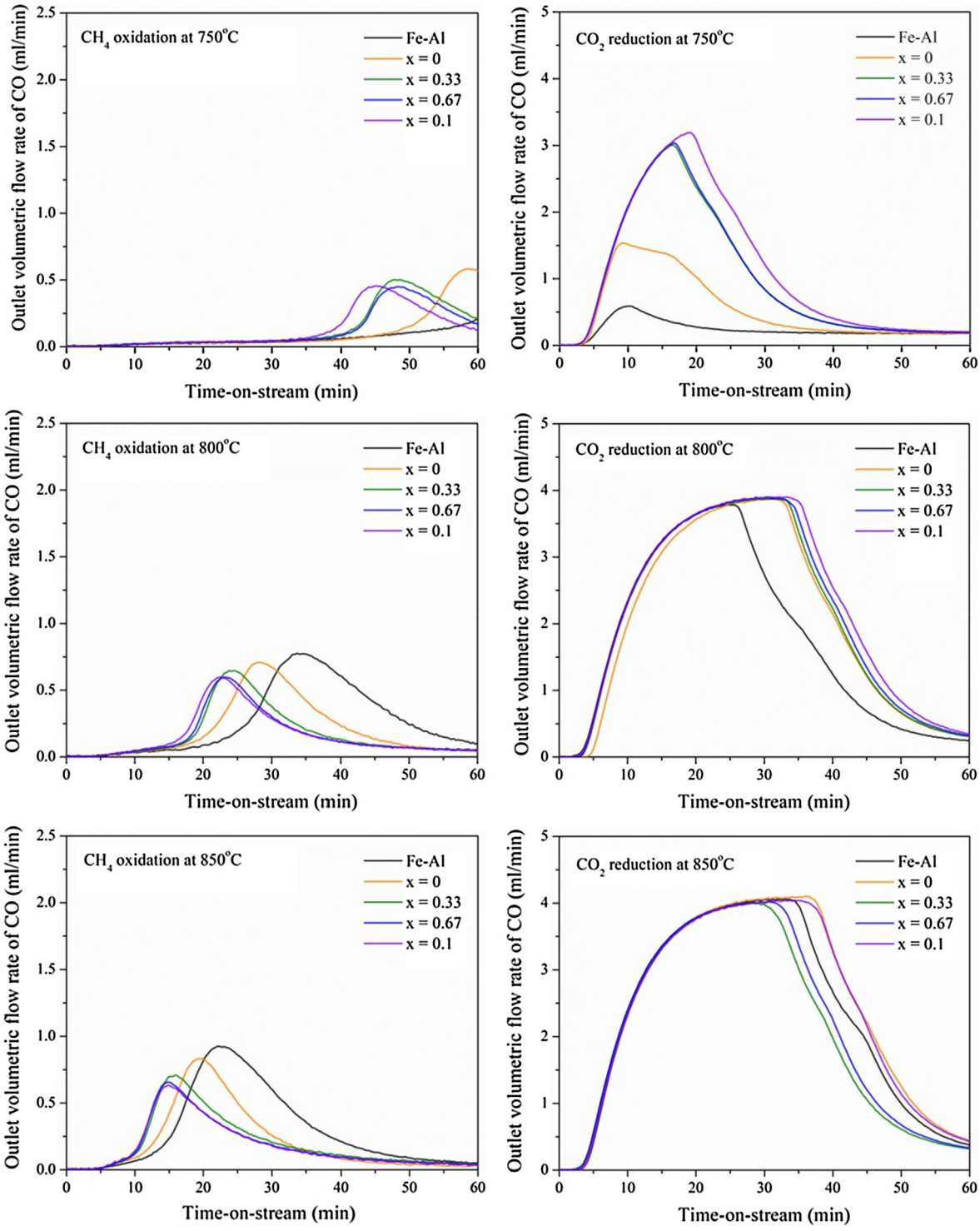

Fig. 2. CO evolution trajectory during the CH_4 oxidation and the CO_2 reduction steps (Temperature: 750, 800, and 850 °C. Flow rate: 2 ml/min of CH_4; 2 ml/min of CO_2; 20 ml/min of He. Gas hourly space velocity: 13200 $cm^3/(g_{cat}·h)$. Time-on-stream: 60 min).

of Fe_2O_3/Al_2O_3 is possibly due to the formation of spinel $FeAl_2O_4$ which possesses a lower oxygen storage capacity than Fe_2O_3. It was reported that the $FeAl_2O_4$ formation may originate from the difficulty in returning the Fe species in Fe_3O_4 (Fe^{2+} in tetrahedral sites and Fe^{3+} in octahedral sites) to the Fe_2O_3 state under CO_2 atmosphere [54]. Meanwhile, an increase in CH_4 conversion with cycle number on the profiles of Fe_2O_3/Al_2O_3 and the modified catalyst (x = 0) is indicative of the noticeable formation of deposited carbon derived from CH_4 pyrolysis. Therefore, the loss of available lattice oxygen is probably due to the blockage of active sites by the accumulated unremovable deposited carbon [19], which inhibits the catalyst activity toward syngas evolution via POM. By contrast, the mild variation of CH_4 conversion and CO selectivity on the profiles of the three La-modified catalysts implies that these catalysts exhibit promising carbon-tolerance and oxygen mobility which secures the overall catalyst stability during cyclic CLDR operation.

Moreover, the non-accumulated carbon deposition (i.e., deposited carbon during CH_4 oxidation step of each cycle) and available

oxygen for CH_4 oxidation were calculated and plotted in related to the cycle number (Fig. 3). It can be found that the available oxygen of Fe_2O_3/Al_2O_3 underwent a remarkable loss after the 1st cycle use and followed by a continuous descending for the subsequent cycles. Accordingly, the carbon deposition on Fe_2O_3/Al_2O_3 became a critical concern and started to surmount the modified catalysts (x = 0 and 0.33) from the 2nd cycle. Unlike Fe_2O_3/Al_2O_3, the La-modified catalysts (x = 0.67 and 1) show significant carbon deposition at each cycle but far less variation of available oxygen for CH_4 oxidation. In the case of the modified catalysts (x = 0 and 0.33) with high-Ce-low-La content, less carbon deposition and mild variation of available oxygen for CH_4 oxidation suggest the Ce presence has a high carbon-resistance.

Now that the carbon-tolerance of La-modified catalysts and carbon-resistance of Ce-modified catalysts show similar CH_4 oxidation performance but the different extent of carbon deposition, we wonder how the deposited carbon affects the CO_2 reduction during the catalyst regeneration process. First, there were two assumptions made: (a) the deposited carbon (i.e., theoretically calculated values of non-accumulated carbon deposition in Fig. 3) can be entirely removed by CO_2, and (b) the available oxygen consumed for both COM and POM during CH_4 oxidation can be fully recovered from CO_2 via CS reaction during CO_2 reduction. Therefore, the calculated CO evolution which is contributed by carbon removal and CS reaction is presented and compared with the measured CO evolution value based on mass spectrometer signal

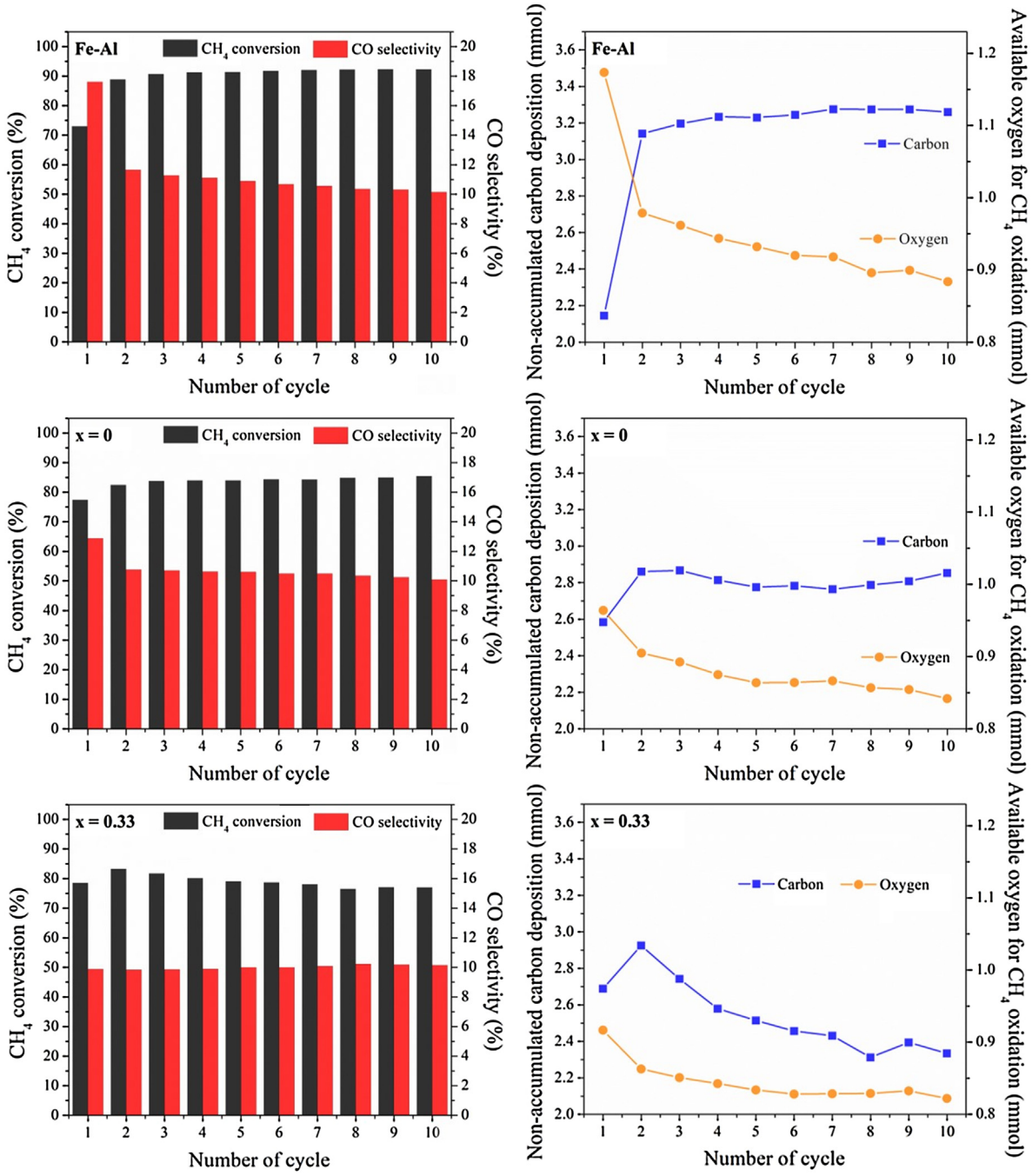

Fig. 3. CH_4 conversion, CO selectivity, non-accumulated carbon deposition and available oxygen for the CH_4 oxidation step of each CLDR cycle. (Temperature: 800 °C. Flow rate: 2 ml/min of CH_4; 20 ml/min of He. Gas hourly space velocity: 13200 $cm^3/(g_{cat}\cdot h)$. Time-on-stream of each CH_4 oxidation step: 60 min. Cycle number: 10).

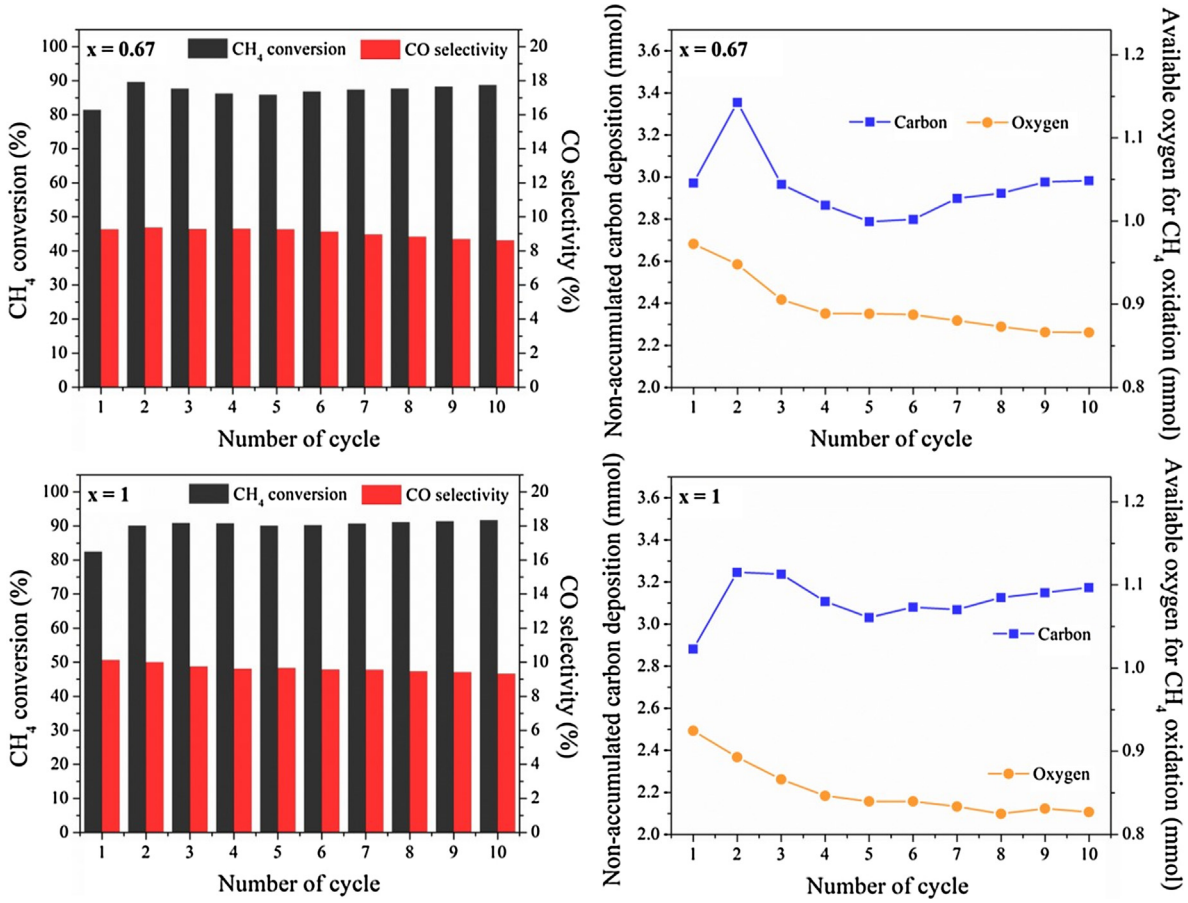

Fig. 3 (*continued*)

readings (Fig. 4). Approximately, the deviation of calculated CO evolution from the measured values is minor and tends to converge as the cycle number increases. Since carbon removal using CO_2 dramatically contributes to the evolution of CO during CO_2 reduction, it is reasonable to speculate that carbon deposition has a more significant impact on the stability of catalyst performance during the first several cycles than the subsequent cycles. Fig. S3-C shows the surface morphology of the modified catalyst (x = 0.33) after the 10th CH_4 oxidation, which indicates whisker-like carbon deposition all over the catalyst surface. In general, there are two kinds of deposited carbon from CH_4 pyrolysis, amorphous carbon and graphitic carbon, respectively. While CO_2 can eliminate the former, the latter has longer filaments and distance from the oxygen-depleted active sites and thereby is inert to CO_2 which shows a lot lower oxidizing ability than O_2. Hence, it is indeed vital to increase the adsorption and activation of CO_2 not only to accelerate the gasification of surface active carbons but also retard the formation of inactive carbon [18,19].

Fig. 4 also shows the variation of CO_2 conversion and CO selectivity toward oxygen replenishment via CS reaction with cycle number. After the 1st cycle, there appeared a significant decline in CO selectivity toward CS on the Fe_2O_3/Al_2O_3 profile while accompanied by an increase in CO_2 conversion. It merits notification that under the same experimental conditions the loss of available oxygen for CH_4 oxidation induces more carbon deposition which subsequently greatly contributes to the increase in CO_2 conversion but results in the reduced CO_2 consumption for oxygen replenishment of catalyst. Benefiting from the improved carbon-resistance and carbon-tolerance, a mild variation of CO_2 conversion and CO selectivity toward CS is perceivable on the profiles of the modified catalysts during the CO_2 reduction steps throughout the entire 10-cycle CLDR operation. Among all the examined catalysts, the modified catalyst (x = 0.33) gives the lowest CO_2 conversion (66.96%) and the highest CO selectivity toward CS reaction (14.97%) during the 10th cycle of CO_2 reduction. In comparison to the modified catalyst (x = 0.33), an increase in Ce or La loading can give rise to the CO_2 conversion via carbon removal instead of CS reaction. Hence, the La/Ce composition in the modified catalyst (x = 0.33) is exceptional, which leads to the promising stability during cyclic CLDR operation concerning the favored POM and CS reactions. Also, by comparing the surface morphology of the modified catalyst (x = 0.33) at the fresh stage (Fig. S3-B) and after the 10th cycle of CO_2 reduction (Fig. S3-D), the minor variation of particle size reflects an effective catalyst resistance toward thermal sintering during the successive high-temperature redox operation.

3.2. Surface characterization of La_xCe_{1-x}-Fe_2O_3/Al_2O_3 redox catalysts

Table 1 shows the effect of La and Ce loading on the BET surface area and BJH pore volume of Fe_2O_3/Al_2O_3. Compared with the Fe_2O_3/Al_2O_3, the sole Ce-addition shows a negligible variation of the specific surface area but improved pore volume by 21.5%. It is noteworthy that the collapse of the porous structure of Fe_2O_3/Al_2O_3 during the elevated-temperature calcination may be inevitable. Although CeO_2 is beneficial to the dispersion of active phase [18,21], the limited thermal sintering-resistance of CeO_2 particles is of great concern which has an adverse impact on the surface area [20,51]. Moreover, higher Ce-loading (Ce/Fe > 1:4) may yield a relatively higher specific surface areaowing to the absence of hematite-like solid solution [47], but overloaded Ce additives

would result in not only the aggregation of CeO_2 but also the pore blockage [48,55] which impairs the catalyst activity and its mechanical strength [42,50]. A decrease in the Ce content while an increase in La-loading remarkably improves the surface area and develops the porous structure of Fe_2O_3/Al_2O_3. Among the La-loaded catalysts, the modified catalyst (x = 0.33) exhibits the largest specific surface area (56.213 m^2/g) and the highest pore volume (0.291 cm^3/g), favoring the diffusion and penetration of reactant gases into the bulk phase. Also, the scanning electron microscopy (SEM) images (Figs. S3-A and S3-B) suggest a significantly reduced average particle size on the fresh modified catalyst (x = 0.33) when compared with the fresh Fe_2O_3/Al_2O_3.

Fig. 5 presents the pore size distribution for the fresh catalysts. While Fe_2O_3 and the solely Ce-loaded catalyst (x = 0) are lack of porous structures, the La-modified catalysts show two prominent peaks (20–50 Å and 50–500 Å) both reflecting strong mesoporous characteristics. The difference among the three La-modified catalysts resides in that lower La-loading preferentially gives the higher distribution of mesopores with smaller pore size, probably due to the CeO_2-benefited higher dispersion of active phase. Table 1 also gives the H_2-chemisorption results of the fresh catalysts, among which the modified catalyst (x = 0.33) exhibits outstandingly the largest active metal surface area (0.694 m^2/g_{cat}), the highest surface metal dispersion (7.938%), the smallest average crystalline size (145.352 Å), and the largest monolayer uptake of H_2 (9.393 μmol/g_{cat}). Again, the H_2-chemisorption results show the Ce-loading is advantageous for surface dispersion of active metal species thereby enhancing the carbon-resistance of catalyst

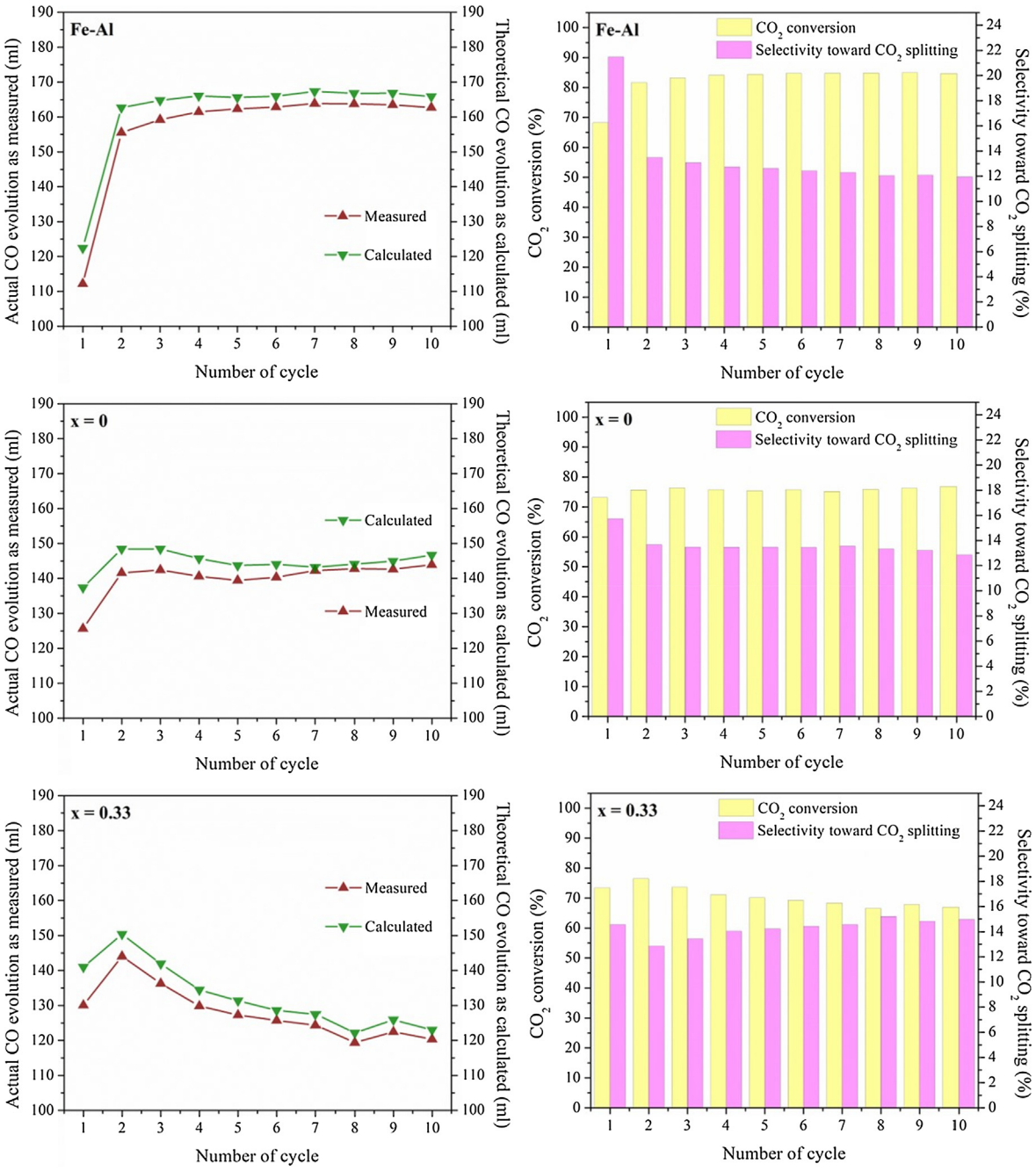

Fig. 4. Deviation of calculated CO evolution from the measured value, CO_2 conversion and reaction selectivity toward CO_2 splitting for the CO_2 reduction step of each CLDR cycle. (Temperature: 800 °C. Flow rate: 2 ml/min of CO_2; 20 ml/min of He. Gas hourly space velocity: 13200 $cm^3/(g_{cat}\cdot h)$. Time-on-stream of each CO_2 oxidation step: 60 min. Cycle number: 10).

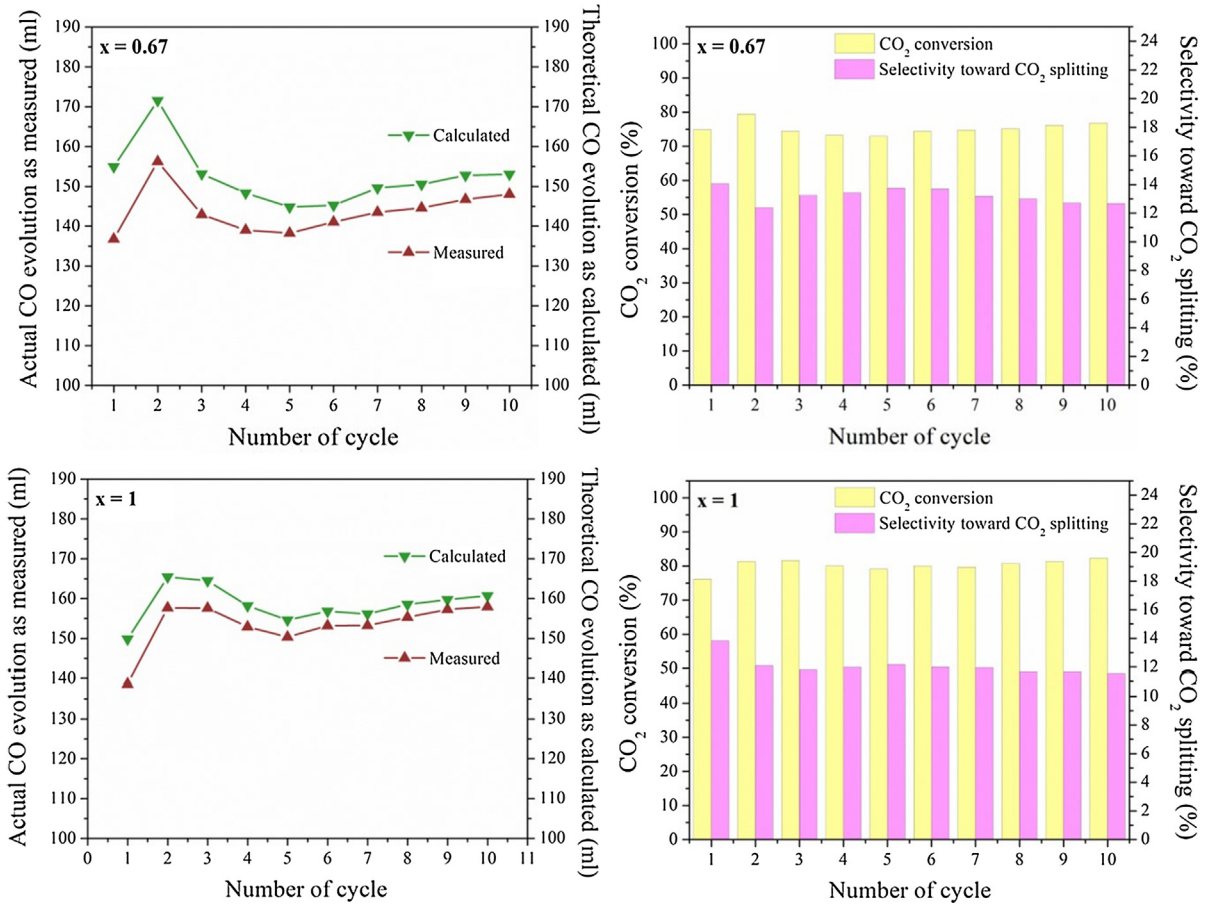

Fig. 4 (*continued*)

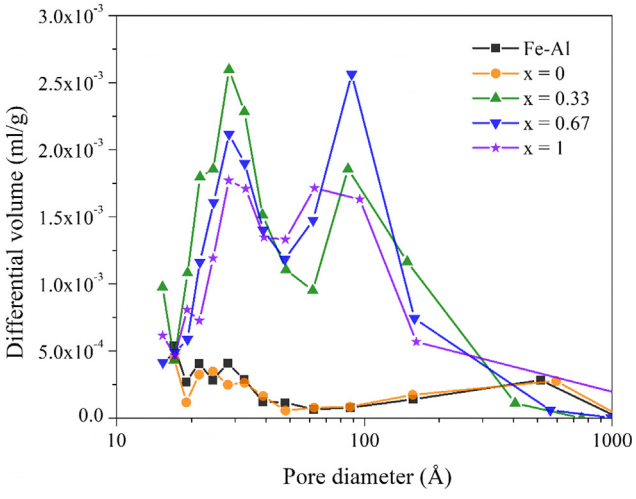

Fig. 5. Pore size distributions of the fresh catalysts.

during CH_4 oxidation and efficiently improving the CO_2 activation for carbon removal during CO_2 reduction.

3.3. Redox characterization of La_xCe_{1-x}-Fe_2O_3/Al_2O_3 redox catalysts

The H_2-TPR and CH_4-TPR tests were performed to evaluate the catalyst reducibility (Fig. 6). In the case of H_2-TPR (Fig. 6A), two peaks (α and β_0) appearing on the profile of Fe_2O_3/Al_2O_3 can be ascribed to the reduction of surface-adsorbed oxygen that is overlapped by the phase transition from Fe_2O_3 to Fe_3O_4, and that from Fe_3O_4 to either FeO or Fe [45,47,48], respectively. After the sole Ce-modification, peak β_1 refers to the overlapping of the reduction of surface CeO_2 and the phase transition from Fe_3O_4 to FeO [45]. While, on the profiles of the La-modified catalysts, both peak β_2 and β_3 correspond to the reduction of bulk Fe^{3+} [42]. The appearance of the γ phase on the profile of the modified catalyst (x = 0) roughly at 900 °C is indicative of the formation of $CeFeO_3$ phase when the catalyst is reduced beyond FeO [45], however, results in a decrease in the catalyst reducibility. Comparably, the high-temperature shift of the α peak upon La-modification is probably due to an increased La-Fe interaction which also is disadvantageous for catalyst reducibility. A similar conclusion can be drawn based on the evolution peaks of CO_2 and CO on the CH_4-TPR profiles (Fig. 6B). The CO_2 evolution via COM is represented by two peaks which can be attributed to the presence of two kinds of oxygen species with different activities toward CH_4. The reactivity strength of the oxygen species is reflected in the form of peak temperature. Corresponding to peak definition in the discussion of H_2-TPR results, the two CO_2 evolution peaks can be correlated to the surface-adsorbed oxygen, and phase transition of $Fe_2O_3 \rightarrow Fe_3O_4$ which favors CO_2 formation via COM, respectively. Also, the CO evolution peak refers to the reaction between CH_4 and POM-favored lattice oxygen via the catalyst reduction beyond Fe_3O_4. Although the catalyst reducibility is impaired due to the presence of Ce-Fe and La-Fe interactions, the evolution peaks of both CO_2 and CO via the reduction of catalyst shift to lower temperatures, suggesting an enhanced lattice oxygen mobility which can also be translated into an improved catalyst activity and the reduced activation energies for COM and POM reactions.

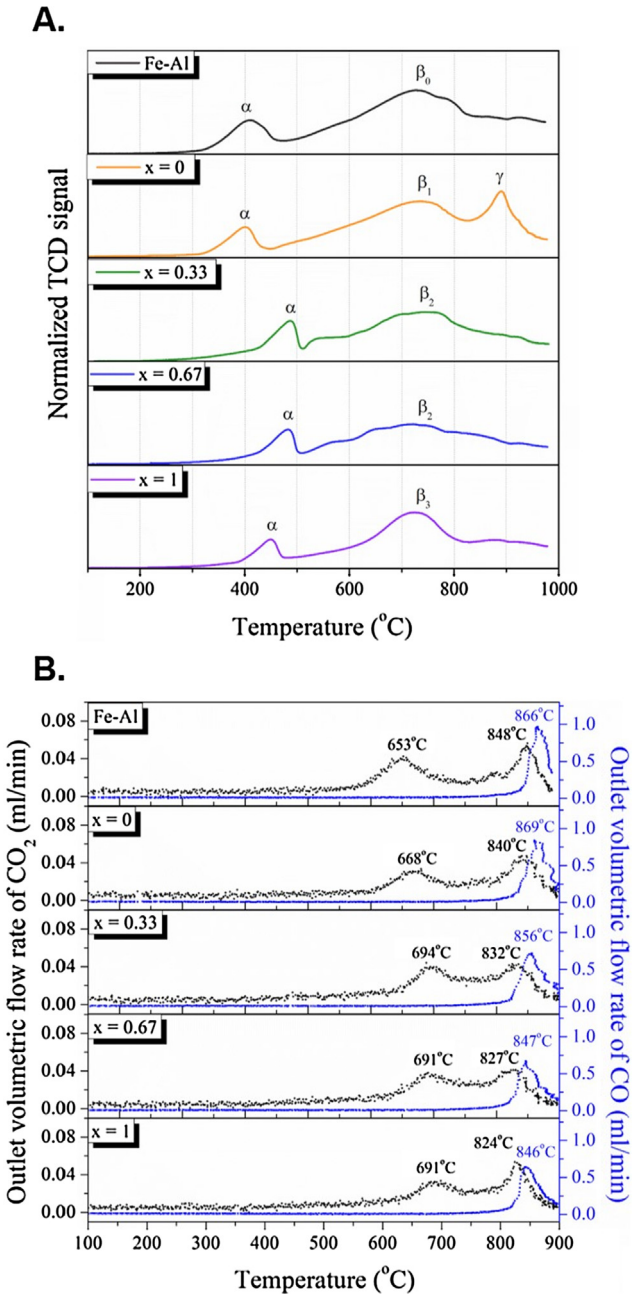

Fig. 6. Evaluation of catalyst reducibility. (A) H_2-TPR profiles of the prepared catalysts with respect to normalized TCD signal. (B) CH_4-TPR profiles of the prepared catalysts with respect to outlet volumetric flow rates of CO_2 and CO.

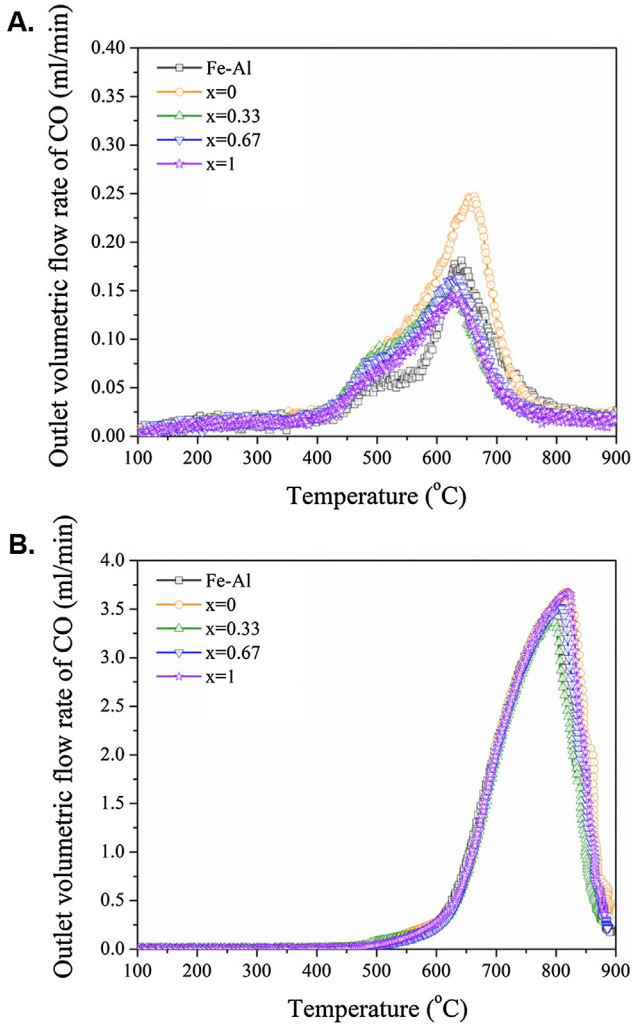

Fig. 7. Evaluation of catalyst oxidizability. CO_2-TPO profiles of the pre-reduced catalysts pre-reduced by using (A) H_2 and (B) CH_4.

The oxidizability of catalysts pre-reduced by H_2 and CH_4 was probed using CO_2-TPO (Fig. 7), which is a measure of the behavioral oxygen transfer at the lattice/surface interface (referred to as intrafacial). In the absence of carbon deposition (Fig. 7A), the CO_2-TPO profiles for all the H_2-reduced catalysts show two oxygen replenishment regions (approximately 450–550 °C and 550–750 °C) both of which via the CS reaction. The difference between these two CO evolution regions with respect to the peak intensity and area lies in the amount of available oxygen defects and active sites as well as the oxygen transfer kinetics of surface lattice (lower-temperature favored) and bulk lattice oxygen (higher-temperature favored). By tailoring the contents of Ce and La additives, the Ce-Fe and La-Fe interactions may essentially impact the oxygen transfer kinetics. In detail, the modified catalyst (x = 0) exhibits the most significant replenishable bulk and surface lattice oxygen, which is possibly owing to the higher surface dispersion of active phase and the more effective surface CO_2 activation. On the CO_2-TPO profiles of the three H_2-reduced La-loaded catalysts, there appears a reduced amount of replenishable surface lattice oxygen and meanwhile a lower amount of replenishable bulk lattice oxygen with higher La-loadings. From the viewpoint of peak temperature, it can be found that La-modification is far more beneficial than Ce-modification to replenishing bulk lattice oxygen at lower temperatures, suggesting a facilitated oxygen transfer owing to the highly active oxygen defects. Moreover, the increase of Ce content in the La-loaded catalysts (x = 0.33 and 0.67) not only further slightly shifts the replenishment of bulk lattice oxygen to a lower temperature but also gives rise to the amount of replenishable of both surface and bulk lattice oxygen. Hence, the simultaneous addition of Ce and La may lead to a synergistic La-Ce effect in the CO_2 regeneration of catalyst via CS reaction.

In comparison to CO_2-TPO of the H_2-reduced catalysts, the far more intensive CO_2 reduction was carried out over the CH_4-reduced catalysts (Fig. 7B), which is primarily affected by the strongly endothermic carbon removal [21,22]. As indicated by the temperature profile, the removal of deposited carbon using CO_2 over all the CH_4 reduced catalysts is thermodynamically favored at the temperature of about 800 °C. Now that the 10-cycle CLDR experiments were also conducted at 800 °C, it is reasonable to speculate that catalyst regeneration via CS may

proceed preferentially rather than carbon removal. Furthermore, it may be inherently necessary for CO_2 molecules to selectively migrate to the most reactive oxygen defects for recovering active sites, prior to CO_2 activation through the formation of oxy-carbonates over regenerated active sites. It is also benefiting from the synergistic La-Ce effect that the carbon removal reaction peaks at the lowest temperature over the CH_4-reduced modified catalyst (x = 0.33) when compared to the other catalysts. Meanwhile, the profile of the CH_4-reduced modified catalyst (x = 0.33) shows the lowest amount of CO formation via carbon removal, which is in accordance with that the modified catalyst (x = 0.33) exhibit the smallest amount of carbon deposition during the 1st cycle of CH_4 oxidation (Fig. 3). Therefore, the simultaneous addition of Ce and La can synergistically improve the carbon-resistance and carbon-tolerance of catalyst, and enhance the CO_2 activation for carbon removal.

3.4. Active phases and reaction pathways determination of La_xCe_{1-x}-Fe_2O_3/Al_2O_3 redox catalysts

Fig. 8 shows the powder XRD diffraction patterns for the fresh catalysts, and the used Fe_2O_3/Al_2O_3 and the modified catalysts (x = 0.33 and 0.67). In Fig. 8A, the XRD pattern of the fresh Fe_2O_3/Al_2O_3 distinctively shows the presence of Fe_2O_3 phase (hematite) (33.12°, JCPDS card No.: 01-072-0469) [12]. Comparably, all the modified catalysts exhibits less peak intensity of the Fe_2O_3 phase, suggesting a reduced Fe_2O_3 crystallinity. Also, the reduction of Fe_2O_3 peak intensity upon the Ce and/or La modification could be attributed to the improved surface dispersion of Fe_2O_3. While the fresh solely Ce-modified catalyst (x = 0) shows the diffraction peak of CeO_2 (28.68°, JCPDS card No.: 00-001-0800), the $LaFeO_3$ phase (32.53°, JCPDS card No.: 01-075-0439) [42] is identified from the diffraction patterns of the La-loaded catalysts. Since there is no

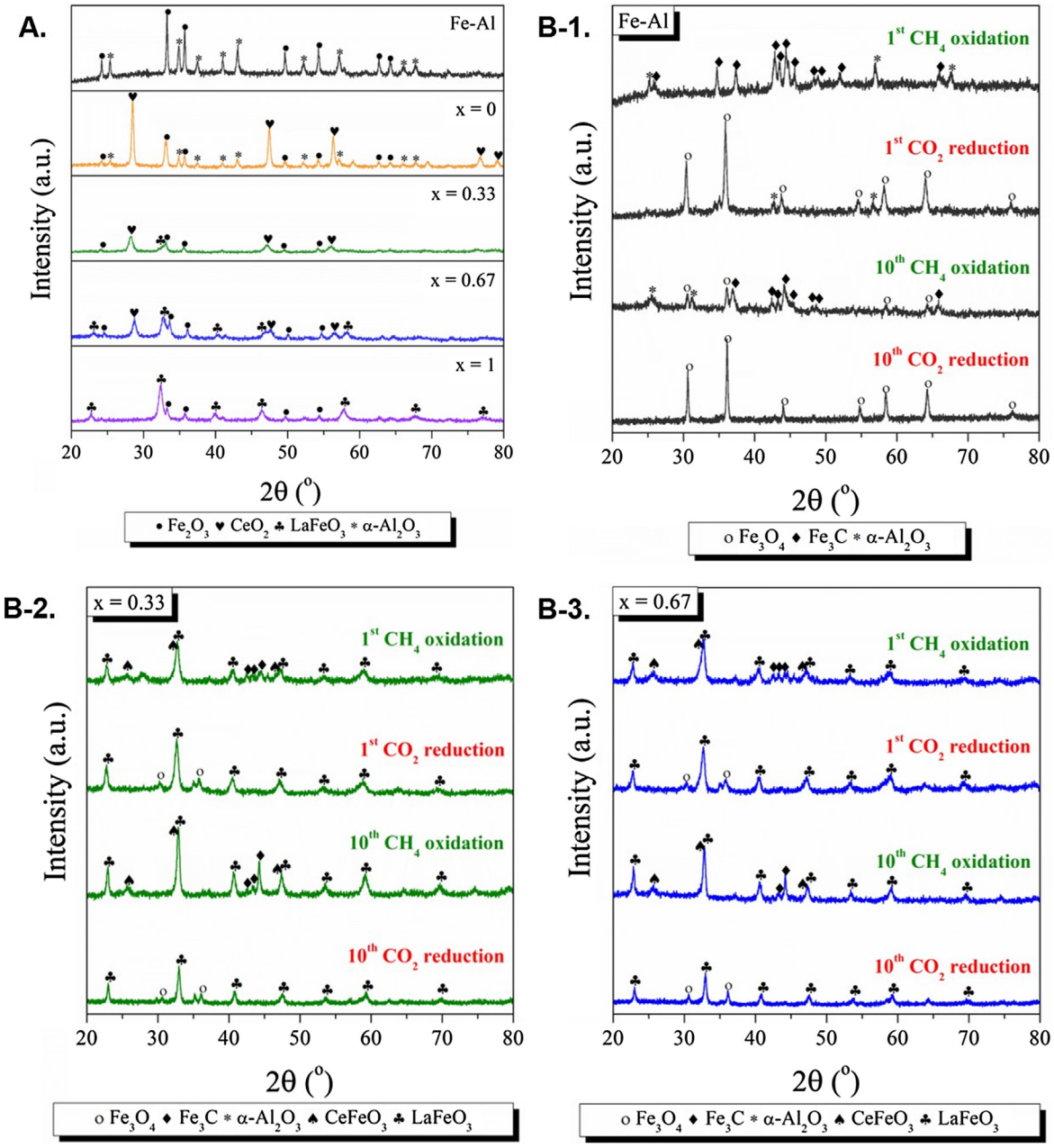

Fig. 8. Powder diffraction patterns for (A) all the fresh catalysts, and (B-1 thru B-3) the used Fe-Al and La_xCe_{1-x}-Fe_2O_3/Al_2O_3 (x = 0.33 and 0.67) at four different redox stages (the 1st CH_4 oxidation, the 1st CO_2 reduction, the 10th CH_4 oxidation, and the 10th CO_2 reduction).

evidence of any separable peak attributions to La_2O_3 (or $La_2(CO_3)_3$) which is known to be rapidly formed at room temperature [51], it should be appropriate to confirm that the La-Fe interaction on the fresh La-modified catalysts is in the form of $LaFeO_3$ that is responsible for the enhanced lattice oxygen mobility. It is also noteworthy that the formation of $LaFeO_3$ during the calcination treatment at 900 °C essentially suppresses the mobility of La species and prevents the evolution of monophasic lanthanum hexaaluminates ($LaAlO_3$) [54,56–58]. Furthermore, the co-existence of Fe_2O_3, CeO_2, and $LaFeO_3$ on the modified catalysts (x = 0.33 and 0.67) may suggest an intimate phase contact, leading to an efficient oxygen migration path during CH_4 oxidation.

After the 1st and the 10th CH_4 oxidation, the reduced Fe_2O_3/Al_2O_3 surface shows a new phase being attributed to Fe_3C (44.93°, JCPDS card No.: 00-006-0686) [12] while the Fe_2O_3 diffraction wholly disappeared (Fig. 8B-1). Since the catalyst regeneration using CO_2 can only incompletely proceed through the phase-transition stages that are reverse to those during the CH_4 oxidation, Fe_3O_4 phase (36.09°, JCPDS card No.: 01-072-6170) appears as the highest achievable oxidation state [12] after the 1st and the 10th CO_2 reduction. In addition, the reason for Fe_3C phase not being perceivable on the Fe_2O_3/Al_2O_3 patterns after catalyst regeneration is possibly due to the lack of crystallinity and high dispersion of graphitic (non-removable) carbon at the catalyst surface.

The surface elemental (O 1s, Fe 2p, Ce 3d, and La 3d) composition and the chemical status of Fe_2O_3/Al_2O_3 and the modified catalysts (x = 0.33 and 0.67) at different stages were characterized using XPS techniques (Fig. S4). The surface oxygen species can be divided into three categories, namely lattice oxygen (529.4 eV, labeled as O_I), surface-adsorbed oxygen (532.2 eV, labeled as O_{II}), and surface hydroxyl and/or carbonate species (533.8 eV, labeled as O_{III}) in an ascending order of the binding energy [50]. Fig. 9A shows the XPS-derived results with respect to the variation of O_{II}/O_I ratio after different cyclic treatments. In the case of Fe_2O_3/Al_2O_3, after the 1st and the 10th cycle of CH_4 oxidation, both lattice oxygen (O_I) and surface-adsorbed oxygen (O_{II}) disappeared on the O 1s spectra, agreeing with the XRD observation that the reduced Fe_2O_3/Al_2O_3 surface is dominated by the Fe_3C coverage. A significant increase in the O_{II}/O_I ratio after catalyst regeneration (the 1st cycle of CO_2 reduction) corresponds to an irreversible loss of the available lattice oxygen for CH_4 oxidation. Comparing the two modified catalysts (x = 0.33 and 0.67), a higher-Ce-lower-La composition leads to a relatively higher surface distribution of lattice oxygen after the 10th cycle of CO_2 reduction as the O_{II}/O_I ratio is lower at the surface of the modified catalyst (x = 0.33). The increase in the availability of lattice oxygen owing to the enhanced surface dispersion not only benefits the syngas production via POM but also effectively improves the catalyst resistance and tolerance to carbon deposition.

The XPS spectra of Fe 2p can be deconvoluted into three peaks, which can be ascribed to the Fe $2p_{3/2}$ (712.5 and 714.9 eV) and Fe $2p_{1/2}$ (725.7 eV) characteristics, respectively [50] (Fig. S4). After the CH_4 oxidation for the three examined catalysts, the Fe $2p_{3/2}$ peak expands in width accompanied by a recession of the shake-up satellite (722.3 eV), indicating the well-defined electron-receiving behavior of surface Fe^{3+} and the corresponding $Fe^{3+} \rightarrow Fe^{2+}$ transition [31]. As further noted from the variation of Fe^{2+}/Fe^{3+} ratio after different cyclic treatment (Fig. 9B), the two modified catalysts (x = 0.33 and 0.67) exhibits higher surface Fe^{2+} distribution than Fe_2O_3/Al_2O_3, again confirming the enhanced lattice oxygen mobility in the Ce- and La-presence.

Now that the phase transition of Fe_2O_3/Al_2O_3 during the cyclic CLDR operation involves the redox relationships among the Fe_2O_3, Fe_3O_4, and Fe_3C phases, the proposed reaction pathway for Fe_2O_3/Al_2O_3 can be expressed as follow:

Fe_2O_3/Al_2O_3 reduction during CH_4 oxidation:

CO_2 evolution via COM [59]:

$$CH_4 + 12Fe_2O_3 \rightarrow CO_2 + 2H_2O + 8Fe_3O_4 \quad (R1)$$

$$CH_4 + 4Fe_3O_4 \rightarrow CO_2 + 2H_2O + 12FeO \quad (R2)$$

$$CH_4 + 4FeO \rightarrow CO_2 + 2H_2O + 4Fe \quad (R3)$$

CO evolution via POM [59]:

$$CH_4 + 3Fe_2O_3 \rightarrow CO + 2H_2 + 2Fe_3O_4 \quad (R4)$$

$$CH_4 + Fe_3O_4 \rightarrow CO + 2H_2 + 3FeO \quad (R5)$$

$$CH_4 + FeO \rightarrow CO + 2H_2 + Fe \quad (R6)$$

Carbon deposition via CH_4 pyrolysis and carbonaceous phase formation [60]:

$$CH_4 \xrightarrow{Fe} C + 2H_2 \quad (R7)$$

$$CH_4 + 3Fe \rightarrow 2H_2 + Fe_3C \quad (R8)$$

Fe_2O_3/Al_2O_3 regeneration during CO_2 reduction:

Fe_3O_4 formation via CS [60]:

$$5CO_2 + Fe_3C \rightarrow 6CO + Fe_3O_4 \quad (R9)$$

$$CO_2 + 3FeO \rightarrow CO + Fe_3O_4 \quad (R10)$$

CO evolution via carbon removal using CO_2 [21,22]:

$$CO_2 + C \rightarrow 2CO \quad (R11)$$

It is intriguing that the carbon formation (R7) and carbon removal (R10) results in an internal cyclic carbon migration, and the resulting reaction coincides with the net reaction of not only the conventional dry reforming reaction but also the proposed CLDR process.

Figs. 8B-2 and 8B-3 show the XRD diffraction patterns of the used modified catalysts (x = 0.33 and 0.67) at different stages. Both modified catalysts exhibit similar diffraction profiles. It was detected that after the CH_4 oxidation the CeO_2 phase is partially reduced to $CeFeO_3$ (32.29°, JCPDS card No.: 00–022-0166), which can improve the durability of CeO_2-Fe_2O_3 and is fairly stable in redox process [55,61]. As shown in Fig. S4, the XPS spectra of Ce 3d can be deconvoluted into two peak categories, v (v, v′, v″, and v‴), and u (u, u′, u″, and u‴), representing the two distinguishable spin–orbit contributions, Ce $3d_{5/2}$ and Ce $3d_{3/2}$, respectively [47]. The doublets of v – u, v″ – u″, and v‴ – u‴ can be assigned to the Ce^{4+} species in the form of CeO_2, and meanwhile, the coupled v′ – u′ peaks refer to the Ce^{3+} species in the form of $CeFeO_3$. Since $CeFeO_3$ solid solution could be obtained through an interfacial contact between CeO_2 and reduced Fe species at elevated temperatures (800–850 °C) in a reducing atmosphere (e.g., CH_4, H_2, and CO) for a short period (less than 2 h) [45,49], the phase transition of $CeO_2 \rightarrow CeFeO_3$ over the two modified catalysts (x = 0.33 and 0.67) can be expressed in the following approaches:

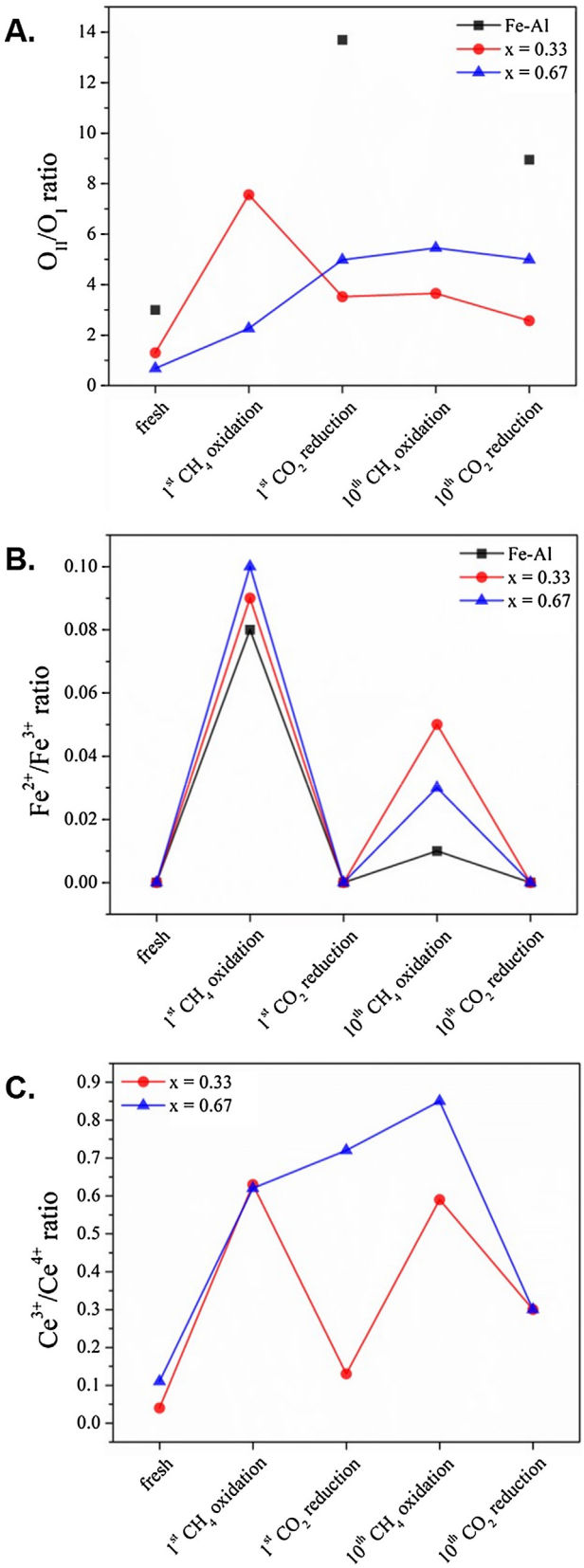

Fig. 9. XPS-derived results reflecting O 1 s, Fe 2p, and Ce 3d on the surface of Fe_2O_3/Al_2O_3 and La_xCe_{1-x}-Fe_2O_3/Al_2O_3 (x = 0.33 and 0.67) in terms of the ratios of (A) O_{II}/O_I, (B) Fe^{2+}/Fe^{3+}, and (C) Ce^{3+}/Ce^{4+} ratios at five different redox stages (fresh, the 1st CH_4 oxidation, the 1st CO_2 reduction, the 10th CH_4 oxidation, and the 10th CO_2 reduction).

$$3CeO_2 + Fe_2O_3 + Fe \rightarrow 3CeFeO_3 \quad (R11)$$

$$CeO_2 + FeO \rightarrow CeFeO_3 \quad (R12)$$

Therefore, a general expression of the redox cycle of the modified catalysts (x = 0.33 and 0.67) can be speculated below:

$$(La_xCe_{1-x} - Fe_2O_3) + \frac{\delta_1}{4}CH_4 \rightarrow \frac{\delta_1}{4}CO_2 + \frac{\delta_1}{2}H_2O + (La_xCe_{1-x} - Fe_2O_{3-\delta_1}) \quad (R13)$$

$$(La_xCe_{1-x} - Fe_2O_{3-\delta_1}) + \delta_2 CH_4 \rightarrow \delta_2 CO + 2\delta_2 H_2 + (La_xCe_{1-x} - Fe_2O_{3-\delta_2}) \quad (R14)$$

$$(La_xCe_{1-x} - Fe_2O_{3-\delta_2}) + 2\delta_3 CO_2 \rightarrow 2\delta_3 CO + (La_xCe_{1-x} - Fe_2O_{3-\delta_4}) \quad (R15)$$

where δ_1, δ_2, δ_3, and δ_4 refer to the sum of surface-adsorbed oxygen and COM-favored lattice oxygen, POM-favored lattice oxygen, and replenished oxygen from CO_2, respectively.

It also should be noted that the $LaFeO_3$ phase with an intact perovskite-type structure is exceptionally stable and therefore remains its XRD characteristics on the diffraction patterns of the modified catalysts (x = 0.33 and 0.67) after successive redox treatments (Figs. 8B-2 and 8B-3). Since Fe^{2+} is not stable in the $LaFeO_3$ structure, the evolution of Fe^{2+} and Ce^{3+} at the CeO_2-$LaFeO_3$ interface may lead to the formation of abundant oxygen defects, facilitating the migration of bulk lattice oxygen to the catalyst surface for syngas production via POM. Thus, it is believed that higher concentrations of Ce^{3+} and Fe^{2+} ions may contribute to more oxygen defects formation [48,50]. However, as evidenced from the XPS results regarding the Fe^{2+}/Fe^{3+} ratio (Fig. 9B) and the Ce^{3+}/Ce^{4+} ratio (Fig. 9C) after the 10th cycle of CH_4 oxidation, a relatively higher Fe^{2+} concentration preferentially appears at the surface of the modified catalyst (x = 0.33), whereas the modified catalyst (x = 0.67) exhibits a higher surface concentration of Ce^{3+} which is in the form of $CeFeO_3$. Therefore, it cannot be simply generalized for Ce^{3+} or Fe^{2+} which merits more oxygen defects that are responsible for rapid oxygen transfer kinetics and effective CO_2 activation.

Since it is possible that dynamic surface reconstruction periodically switches between metal dispersion and metal aggregation during the cyclic CLDR operation, an intimate contact among the active phases of $LaFeO_3$ and $CeFeO_3$ perovskites, CeO_2, Fe oxides, and even Fe_3C over the modified catalysts (x = 0.33 and 0.67) may have a significant interfacial influence on the lattice oxygen transfer which is critical for both the catalyst reduction kinetics and the catalyst resistance to inactive carbon formation. According to the H_2-chemisorption results (Table 1), in the absence of Ce addition, the modified catalyst (x = 1) exhibits the lowest surface dispersion of active phase because of the large-crystalline-size $LaFeO_3$. When a relatively smaller amount of Ce additives over the modified catalyst (x = 0.67) introduces the CeO_2 phase which improves the surface dispersion of $LaFeO_3$, the evolution of new $CeFeO_3$ phase during CH_4 oxidation induces more oxygen defects, however, reduces the availability of lattice oxygen for syngas production via POM (Fig. 3) and replenishable oxygen for CO production via CS (Fig. 4). In addition, compared with the modified catalyst (x = 0.33), the increased surface concentration of $CeFeO_3$ along with the large-crystalline-size $LaFeO_3$ at the surface of the modified catalyst (x = 0.67) may start to aggregate due to a relatively higher shortage of CeO_2, hence suffering from a loss in the catalyst resistance toward inactive carbon formation and the surface dispersion of oxygen defects. In these regards, from an operational viewpoint, a higher-Ce-lower-La composition (x = 0.33) is more promising which aims at a more efficient utilization of lattice

oxygen and a more effective carbon removal for the integrated syngas production.

Moreover, as observed from the TPR results (Fig. 6), the reduction of α peak during H_2-TPR and the CO_2 formation during CH_4-TPR shifted toward higher temperatures after the La-introduction, suggesting that the presence of $LaFeO_3$ has no promoting effect on the surface-adsorbed oxygen nor favors the reduction of Fe_2O_3 to Fe_3O_4. Instead, the presence of La could accelerate the formation of CO during CH_4-TPR and CH_4 oxidation experiments. Since the reduction of Fe_2O_3 to Fe_3O_4 is preferential for the CO_2 formation while the coexistence of Fe^0 and FeO contributed to the CO production [40], it can be inferred that Fe oxide layers may partially cover the $LaFeO_3$ after calcination, and thus $LaFeO_3$ fails to efficiently conduct oxygen for CO_2 formation at the beginning of CH_4 oxidation process (Fig. 6). Upon the reduction of Fe_2O_3 to either FeO or Fe^0, the exposure of $LaFeO_3$ to the reduced Fe species allows lattice oxygen to migrate from the $LaFeO_3$ structure to the lower valence Fe species and subsequently react with CH_4 to form CO on the surface of Fe species. After the release of oxygen, oxygen defects are formed in the structure of $LaFeO_3$ and can be refilled with oxygen from oxidized Fe and Ce species in bulk. Therefore, as CH_4 oxidation proceeds, the bulk oxygen can be continuously conveyed to the surface through the oxygen vacancies paved paths in $LaFeO_3$ and readily participate in the reaction. Similarly, in Fe oxide-lanthanum strontium ferrite core-shell catalysts [40], the Fe oxide was a primary source of the lattice oxygen, while the perovskite shell accelerated the oxygen conduction and provided the active sites for CH_4 oxidation. Different from the core-shell catalysts, the prepared La_xCe_{1-x}-Fe_2O_3/Al_2O_3 (x = 0.33 and 0.67) catalysts are composites comprising of Fe_2O_3, CeO_2, and $LaFeO_3$ perovskite type oxides, enabling an intimate contact among these species and thereby a possible increase in the formation of active $LaFeO_3$ perovskites. It was reported in the literature that when the surface oxygen concentration is lower than that in bulk, oxygen transportation from bulk to the surface is the rate-determining step for CH_4 oxidation [44]. In these regards, $LaFeO_3$ is of critical catalytic importance in the lattice oxygen mobilization from bulk to surface for the overall redox operation. Similarly, the formation of $CeFeO_3$ during CH_4 oxidation also contributes to the enhancement of oxygen mobility and thereby the decrease in the activation barrier. Hence, both $LaFeO_3$ and $CeFeO_3$ play the catalytic role in accelerating the redox behavior of oxidized Fe species and act as oxygen conduction media. In comparison to $LaFeO_3$- and $CeFeO_3$-present catalysts, due to the limited accessibility of lattice oxygen over Fe_2O_3/Al_2O_3, Fe_2O_3/Al_2O_3 has a significantly restricted oxygen mobility, and thus leads to a longer residence time for POM.

4. Conclusions

This work contributes to an understanding of the synergistic La-Ce effect over the synthesized La_xCe_{1-x}-Fe_2O_3/Al_2O_3 (x = 0.33 and 0.67) composites on the optimized syngas production via a proposed CLDR process. The synergistic La-Ce effect resides in the intimate contact among the active phases including $LaFeO_3$, $CeFeO_3$, CeO_2, Fe oxides, and Fe_3C. While both the $LaFeO_3$ and $CeFeO_3$ perovskites give abundant oxygen defects facilitating lattice oxygen transfer kinetics, the presence of CeO_2 over the catalysts benefits the surface dispersion of active phases and oxygen defects. Owing to the synergistic La-Ce effect, the resistance of catalyst toward aggregation and inactive carbon formation gets enhanced, which further warrants the promising catalyst tolerance against deposited carbon from the continuous cyclic operation and assures the effective CO_2 activation for not only the replenishment of lattice oxygen but also the removal of deposited carbon. Acting as an intermediate material, the CH_4 pyrolysis-induced carbon deposition greatly contributes to an intensive CO_2 reduction, and the carbon migration sharing the same net reaction with the proposed CLDR process may essentially constitute a sub-cycle that merits in-depth study. Future efforts should also consider developing La-Ce composites with ordered porous structures without sacrificing the intimate contact among the active phases.

Acknowledgements

The authors would like to gratefully acknowledge the State of Wyoming and National Science Foundation (NSF 1632899 and NSF 1604630) for the financial supports of this research.

Appendix A. Supplementary material

Supplementary data to this article can be found online at https://doi.org/10.1016/j.jcat.2018.09.022.

References

[1] S.I. Seneviratne, M.G. Donat, A.J. Pitman, R. Knutti, R.L. Wilby, Allowable CO_2 emissions based on regional and impact-related climate targets, Nature 529 (2016) 477–483.
[2] J. Rogelj, M. den Elzen, N. Höhne, T. Fransen, H. Fekete, H. Winkler, R. Schaeffer, F. Sha, K. Riahi, M. Meinshausen, Paris agreement climate proposals need a boost to keep warming well below 2 °C, Nature 534 (2016) 631–639.
[3] O. Boucher, V. Bellassen, H. Benveniste, P. Ciais, P. Criqui, C. Guivarch, H. Le Treut, S. Mathy, R. Séférian, Opinion: in the wake of paris agreement, scientists must embrace new directions for climate change research, Proc. Natl. Acad. Sci. USA 113 (2016) 7287–7290.
[4] H.J. Schellnhuber, S. Rahmstorf, R. Winkelmann, Why the right climate target was agreed in paris, Nat. Clim. Chang. 6 (2016) 649–653.
[5] P. Friedlingstein, R.M. Andrew, J. Rogelj, G.P. Peters, J.G. Canadell, R. Knutti, G. Luderer, M.R. Raupach, M. Schaeffer, D.P. van Vuuren, C. Le Quéré, Persistent growth of CO_2 emissions and implications for reaching climate targets, Nat. Geosci. 7 (2014) 709–715.
[6] B. Li, Y. Duan, D. Luebke, B. Morreale, Advances in CO_2 capture technology: A patent review, Appl. Energy. 102 (2013) 1439–1447.
[7] S.D. Kenarsari, D. Yang, G. Jiang, S. Zhang, J. Wang, A.G. Russell, Q. Wei, M. Fan, Review of recent advances in carbon dioxide separation and capture, RSC Adv. 3 (2013) 22739–22773.
[8] B. Dutcher, M. Fan, A.G.A.G. Russell, Amine-based CO_2 capture technology development from the beginning of 2013 – A review, ACS Appl. Mater. Interfaces 7 (2015) (2013) 2137–2148.
[9] G. Shaffer, Long-term effectiveness and consequences of carbon dioxide sequestration, Nat. Geosci. 3 (2010) 464–467.
[10] M.D. Porosoff, B. Yan, J.G. Chen, Catalytic Reduction of CO2 by H2 for Synthesis of CO, Methanol and Hydrocarbons: Challenges and Opportunities, Energy Environ. Sci. 9 (2016) 62–73.
[11] W.-H. Wang, Y. Himeda, J.T. Muckerman, G.F. Manbeck, E. Fujita, CO2 Hydrogenation to Formate and Methanol as an Alternative to Photo- and Electrochemical CO2 Reduction, Chem. Rev. 115 (2015) 12936–12973.
[12] V. Galvita, H. Poelman, C. Detavernier, G. Marin, Catalyst-Assisted Chemical Looping for CO2 Conversion to CO, Appl. Catal. B Environ. 164 (2015) 184–191.
[13] S.N. Habisreutinger, L. Schmidt-Mende, J.K. Stolarczyk, Photocatalytic Reduction of CO2 on TiO2 and Other Semiconductors, Angew. Chemie. 52 (2013) 7372–7408.
[14] B. Han, W. Wei, L. Chang, P. Cheng, Y.H. Hu, Efficient Visible Light Photocatalytic CO2 Reforming of CH4, ACS Catal. 6 (2016) 494–497.
[15] J. Qiao, Y. Liu, F. Hong, J. Zhang, A Review of Catalysts for the Electroreduction of Carbon Dioxide to Produce Low-Carbon Fuels, Chem. Soc. Rev. 43 (2014) 631–675.
[16] A.M. Appel, J.E. Bercaw, A.B. Bocarsly, H. Dobbek, D.L. DuBois, M. Dupuis, J.G. Ferry, E. Fujita, R. Hille, P.J.A. Kenis, C.A. Kerfeld, R.H. Morris, C.H.F. Peden, A.R. Portis, S.W. Ragsdale, T.B. Rauchfuss, J.N.H. Reek, L.C. Seefeldt, R.K. Thauer, G.L. Waldrop, Frontiers, Opportunities, and Challenges in Biochemical and Chemical Catalysis of CO2 Fixation, Chem. Rev. 113 (2013) 6621–6658.
[17] D. Pakhare, J. Spivey, A Review of Dry (CO2) Reforming of Methane over Noble Metal Catalysts, Chem. Soc. Rev. 43 (2014) 7813–7837.
[18] M. Tang, L. Xu, M. Fan, Effect of Ce on 5 wt% Ni/ZSM-5 Catalysts in the CO2 Reforming of CH4 Reaction, Int. J. Hydrogen Energy. 39 (2014) 15482–15496.
[19] L. Xu, L. Duan, M. Tang, P. Liu, X. Ma, Y. Zhang, H. Harris, M. Fan, Catalytic CO2 Reforming of CH4 over Cr-Promoted Ni/Char for H2 Production, Int. J. Hydrogen Energy. 39 (2014) 10141–10153.
[20] S. Bhavsar, G. Veser, Chemical Looping Beyond Combustion: Production of Synthesis Gas via Chemical Looping Partial Oxidation of Methane, RSC Adv. 4 (2014) 47254–47267.

[21] W. Chen, G. Zhao, Q. Xue, L. Chen, Y. Lu, High Carbon-Resistance Ni/CeAlO3-Al2O3 Catalyst for CH4/CO2 Reforming, Appl. Catal. B Environ. 136 (2013) 260–268.
[22] S.A. Theofanidis, V.V. Galvita, H. Poelman, G.B. Marin, Enhanced Carbon-Resistant Dry Reforming Fe-Ni Catalyst: Role of Fe, ACS Catal. 5 (2015) 3028–3039.
[23] L. Neal, A. Shafiefarhood, F. Li, Effect of Core and Shell Compositions on MeOx@LaySr1-yFeO3 Core-Shell Redox Catalysts for Chemical Looping Reforming of Methane, Appl. Energy. 157 (2015) 391–398.
[24] V.L. Sushkevich, D. Palagin, M. Ranocchiari, J.A. van Bokhoven, Selective anaerobic oxidation of methane enables direct synthesis of methanol, Science (80-.) 356 (2017) 523–527.
[25] V. Fleischer, U. Simon, S. Parishan, M.G. Colmenares, O. Görke, A. Gurlo, W. Riedel, L. Thum, J. Schmidt, T. Risse, K.-P. Dinse, R. Schomäcker, Investigation of the role of the Na_2WO_4/Mn/SiO_2 catalyst composition in the oxidative coupling of methane by chemical looping experiments, J. Catal. 360 (2018) 102–117.
[26] M. Najera, R. Solunke, T. Gardner, G. Veser, Carbon capture and utilization via chemical looping dry reforming, Chem. Eng. Res. Des. 89 (2011) 1533–1543.
[27] M.S.C. Chan, E. Marek, S.A. Scott, J.S. Dennis, Chemical looping epoxidation, J. Catal. 359 (2018) 1–7.
[28] S. Bhavsar, M. Najera, G. Veser, Chemical looping dry reforming as novel, intensified process for CO_2 activation, Chem. Eng. Technol. 35 (2012) 1281–1290.
[29] M. Tang, L. Xu, M. Fan, Progress in oxygen carrier development of methane-based chemical-looping reforming: a review, Appl. Energy. 151 (2015) 143–156.
[30] M. Luo, S. Wang, L. Wang, M. Lv, Reduction kinetics of iron-based oxygen carriers using methane for chemical-looping combustion, J. Power Sources 270 (2014) 434–440.
[31] N.L. Galinsky, A. Shafiefarhood, Y. Chen, L. Neal, F. Li, Effect of support on redox stability of iron oxide for chemical looping conversion of methane, Appl. Catal. B Environ. 164 (2015) 371–379.
[32] L. Huang, M. Tang, M. Fan, H. Cheng, Density functional theory study on the reaction between hematite and methane during chemical looping process, Appl. Energy 159 (2015) 132–144.
[33] L.M. Neal, A. Shafiefarhood, F. Li, Dynamic methane partial oxidation using a Fe_2O_3@$La_{0.8}Sr_{0.2}FeO_{3-\delta}$ core-shell redox catalyst in the absence of gaseous oxygen, ACS Catal. 4 (2014) 3560–3569.
[34] S. Chen, L. Zeng, H. Tian, X. Li, J. Gong, Enhanced lattice oxygen reactivity over ni-modified wo_3-based redox catalysts for chemical looping partial oxidation of methane, ACS Catal. 7 (2017) 3548–3559.
[35] H. Sun, L. Cao, L. Lu, Bacteria promoted hierarchical carbon materials for high-performance supercapacitor, Energy Environ. Sci. 5 (2012) 6206–6213.
[36] J. Huang, W. Liu, Y. Yang, B. Liu, High-performance Ni-Fe redox catalysts for selective CH_4 to syngas conversion via chemical looping, ACS Catal. (2018) 1748–1756.
[37] E.R. Monazam, R.W. Breault, R. Siriwardane, Kinetics of magnetite (Fe_3O_4) oxidation to hematite (Fe_2O_3) in air for chemical looping combustion, Ind. Eng. Chem. Res. 53 (2014) 13320–13328.
[38] X. Zhu, K. Li, L.M. Neal, F. Li, Perovskites as geo-inspired oxygen storage materials for chemical looping and three-way catalysis – A perspective, ACS Catal. (2018) 8213–8236.
[39] O. Mihai, D. Chen, A. Holmen, Chemical looping methane partial oxidation: the effect of the crystal size and O content of $LaFeO_3$, J. Catal. 293 (2012) 175–185.
[40] L. Nalbandian, A. Evdou, V. Zaspalis, La1−xSrxMy$Fe_{1-y}O_{3-\delta}$ perovskites as oxygen-carrier materials for chemical-looping reforming, Int. J. Hydrogen Energy. 36 (2011) 6657–6670.
[41] K. Zhao, F. He, Z. Huang, G. Wei, A. Zheng, H. Li, Z. Zhao, Perovskite-type oxides $LaFe_{1-x}Co_xO_3$ for chemical looping steam methane reforming to syngas and hydrogen Co-production, Appl. Energy 168 (2016) 193–203.
[42] K. Zhao, F. He, Z. Huang, A. Zheng, H. Li, Z. Zhao, Three-dimensionally ordered macroporous $LaFeO_3$ perovskites for chemical-looping steam reforming of methane, Int. J. Hydrogen Energy 39 (2014) 3243–3252.
[43] L. Qin, Z. Cheng, M. Guo, M. Xu, J.A. Fan, L.-S. Fan, Impact of 1% lanthanum dopant on carbonaceous fuel redox reactions with an iron-based oxygen carrier in chemical looping processes, ACS Energy Lett. 2 (2017) 70–74.
[44] O. Mihai, D. Chen, A. Holmen, Catalytic consequence of oxygen of lanthanum ferrite perovskite in chemical looping reforming of methane, Ind. Eng. Chem. Res. 50 (2011) 2613–2621.
[45] X. Zhu, Y. Wei, H. Wang, K. Li, Ce–Fe oxygen carriers for chemical-looping steam methane reforming, Int. J. Hydrogen Energy. 38 (2013) 4492–4501.
[46] B. Goris, S. Turner, S. Bals, G. Van Tendeloo, Three-dimensional valency mapping in ceria nanocrystals, ACS Nano. 8 (2014) 10878–10884.
[47] Z. Gu, K. Li, S. Qing, X. Zhu, Y. Wei, Y. Li, H. Wang, Enhanced reducibility and redox stability of Fe_2O_3 in the presence of CeO_2 nanoparticles, RSC Adv. 4 (2014) 47191–47199.
[48] H. Liang, Study on the effect of CeO_2 on Fe_2O_3/$LaNiO_3$ as the oxygen carrier applied in chemical-looping hydrogen generation, Int. J. Hydrogen Energy 40 (2015) 13338–13343.
[49] K. Li, H. Wang, Y. Wei, D. Yan, Syngas production from methane and air via a redox process using Ce–Fe mixed oxides as oxygen carriers, Appl. Catal. B Environ. 97 (2010) 361–372.
[50] Y. Zheng, K. Li, H. Wang, D. Tian, Y. Wang, X. Zhu, Y. Wei, M. Zheng, Y. Luo, Designed oxygen carriers from macroporous $LaFeO_3$ supported CeO_2 for chemical-looping reforming of methane, Appl. Catal. B Environ. 202 (2017) 51–63.
[51] S. Bhavsar, N. Isenberg, A. More, G. Veser, Lanthana-doped ceria as active support for oxygen carriers in chemical looping combustion, Appl. Energy 168 (2016) 236–247.
[52] F. He, F. Li, Perovskite promoted iron oxide for hybrid water-splitting and syngas generation with exceptional conversion, Energy Environ. Sci. 8 (2015) 535–539.
[53] H. Choi, A. Fuller, J. Davis, C. Wielgus, U.S. Ozkan, Ce-doped strontium cobalt ferrite perovskites as cathode catalysts for solid oxide fuel cells: effect of dopant concentration, Appl. Catal. B Environ. 127 (2012) 336–341.
[54] Y. Zhu, W. Liu, X. Sun, X. Ma, Y. Kang, X. Wang, J. Wang, La-hexaaluminate for synthesis gas generation by chemical looping partial oxidation of methane using CO_2 as sole oxidant, AIChE J. 64 (2018) 550–563.
[55] N.V.R.A. Dharanipragada, M. Meledina, V.V. Galvita, H. Poelman, S. Turner, G. Van Tendeloo, C. Detavernier, G.B. Marin, Deactivation study of Fe_2O_3–CeO_2 during redox cycles for CO production from CO_2, Ind. Eng. Chem. Res. 55 (2016) 5911–5922.
[56] Y. Zhang, X. Wang, Y. Zhu, X. Liu, T. Zhang, Thermal evolution crystal structure and fe crystallographic sites in $LaFe_xAl_{12-x}O_{19}$ hexaaluminates, J. Phys. Chem. C. 118 (2014) 10792–10804.
[57] S. Royer, D. Duprez, F. Can, X. Courtois, C. Batiot-Dupeyrat, S. Laassiri, H. Alamdari, Perovskites as substitutes of noble metals for heterogeneous catalysis: dream or reality, Chem. Rev. 114 (2014) 10292–10368.
[58] M. Tian, X.D. Wang, T. Zhang, Hexaaluminates: a review of the structure, synthesis and catalytic performance, Catal. Sci. Technol. 6 (2016) 1984–2004.
[59] Q. Imtiaz, N.S. Yüzbasi, P.M. Abdala, A.M. Kierzkowska, W. van Beek, M. Broda, C.R. Müller, Development of $MgAl_2O_4$-stabilized, Cu-doped, Fe_2O_3-based oxygen carriers for thermochemical water-splitting, J. Mater. Chem. A. 4 (2016) 113–123.
[60] H. Wang, G. Li, J. Ma, D. Zhao, The effect of methane decomposition on the formation and magnetic properties of iron carbide prepared from oolitic hematite, RSC Adv. 7 (2017) 3921–3927.
[61] X. Zhu, H. Wang, Y. Wei, K. Li, X. Cheng, Hydrogen and syngas production from two-step steam reforming of methane over CeO_2-Fe_2O_3 oxygen carrier, J. Rare Earths 28 (2010) 907–913.